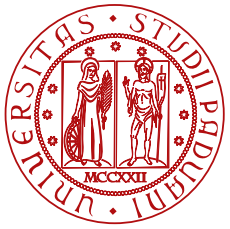

Università degli Studi di Padova

Dipartimento di Ingegneria dell'Informazione

Master Thesis in Control System Engineering

Kalman filtering for temperature estimation of electric motors

Master Candidate

Samira Carolina Sánchez El Ryfaie

Student ID 2018619

Supervisor

Prof. Mattia Bruschetta

University of Padova

Co-supervisor

Prof. Ruggero Carli

University of Padova

Academic Year
2021/2022

Abstract

Due to their high power density and good efficiency, permanent magnet synchronous machines (PMSM) have been increasingly employed in medium-power applications such as vehicular propulsion (electrical/hybrid vehicles), industrial drives and power generation. Since high temperatures can significantly shorten the lifetime of the motor components, there is a growing trend towards real-time monitoring of the internal temperatures during operation. Therefore, the temperature at some key points within the motor needs to be measured to guarantee optimal utilization of the machine, i.e. maximizing its efficiency while assuring safer operation modes. While the stator temperature can be easily accessed by embedding thermal sensors, rotor temperatures are difficult to measure in practice. As an alternative to conventional direct/indirect measurement approaches, model-based methods have been investigated in the past decades. In this work, the feasibility of using the Kalman algorithm is investigated, as a thermal observer for temperature estimation.

Contents

List of Figures

List of Tables

List of Algorithms

1 Introduction

This work presents the design, application, and evaluation of a Kalman filter algorithm, based on a thermal model solved by the Finite Element Method (FEM), as a thermal observer for temperatures estimation in an electric motor. This research is part of an applied research project aimed at future industrial applications of Digital Twins for monitoring, control optimisation and predictive maintenance of this type of devices and fits into the relentless trend toward electric vehicles and cleanest electric power generation (wind, waves, hydro and nuclear). Due to their high-power density and good efficiency, permanent magnet synchronous machines (PMSM) have been increasingly employed in several industrial applications, including medium-power applications such as vehicular propulsion (electrical/hybrid vehicles), industrial drives and power generation [5]. However, under working conditions (particularly in the case of motors) the temperatures of such devices can rise (due to friction and ohmic heating), and then significantly shorten the lifetime of the motor components (mainly the permanent magnets but also others as attached/embedded electronic circuitt's components and plastic isolators). This is one of the main reasons boosting the growing trend towards real-time monitoring of the internal temperatures during operation. Therefore, the temperature at some key points within the motor needs to be measured to guarantee optimal utilization of these machines. This redounds in maximizing its efficiency, allows to extend the operational cycles, also extends the life span of the machines, while assuring safer operation modes. However, among the different parts of the motors, some are easily accessible, though not all. For instance, while the stator temperature can be

easily accessed by standard embedding thermal sensors, rotor temperatures are difficult to measure in practice, since the installation of a thermal sensor there is a difficult task. In this context, model-based methods have been investigated in the past decades, as an alternative to conventional direct/indirect measurement approaches, accumulating a considerable experience that contributes to what we now call Digital Twins. In particular, estimators for electrical motor temperatures have been presented for engineering applications [20], [6], [21], [22], [10] using different strategies.

In the present work, a Kalman filter is proposed and implemented in order to assess the feasibility of using this strategy to develop an improved thermal observer, which eventually can be used for permanent magnet synchronous motors, even in presence of input uncertainties. The motor model consists of a Finite Element representation of the corresponding physical thermal transport equations after applying an order reduction method. On the other hand, it is well known that in the case of complex systems (geometry, diversity of constituent materials, changing parameters of those materialt's properties, etc.), models of high complexity are required to obtain a proper description of the physical system. Doing that, it is generally assumed similitude between the real system and the model, and between the testing and operational conditions. Then, the models must be devised with the best-physics approach that is relevant to each particular machine [8].

Due to the motor model complexity, we decided to take two steps back and start studying a rather simple system to test first the Kalman filter. We chose then to start with a simple homogeneous solid bar model, which could be formulated using the same methods as in the motor model but having a simpler structure. Once developed the desired robust temperature observer for the bar; this solution was scaled until reaching the ultimate goal, which is the development of a robust temperature observer that can be used for simulating, monitoring and optimizing the permanent magnet synchronous motors. In Chapter 2 the Heat Transfer Model is described, along with the used strategies required for its Finite Element Method (FEM) solution, which are the space domine discretization and the formulation of the problem in its strong and weak forms, to finally obtain a linear model allowing the construction of an approximate solution for the analysed thermal models. It was applied to the metal bar model and to the electric motor model, to this last it was also used an order reduction method (in a previous work) to be able to run the designed algorithms in an efficient way

[13]. The model time discretization is also presented within this chapter since it is necessary to solve the FEM problem.

The Kalman filter main aspects are discussed in Chapter 3, where the arguments for using an offset-free Linear Kalman filter are exposed, while the Kalman filter implementation to both models (the bar model and the motor model) is shown in Chapter 4 where the main results of this work are presented. It is worth noticing that the classic Kalman filter has some limitation in the case of uncertain input conditions, so an augmented state Kalman filter was applied to overcome these situations. Finally, both are compared and quantitative results on their performance under different conditions and using different positions for the read back sensors are discussed.

2

The Heat Transfer Model

The physical phenomena related to electric motors (mechanics, electromagnetism, thermodynamics, etc.) can be modeled by partial differential equations (PDEs). Those systems are often featured by complex geometries, possibly involving different materials, which implies complex border conditions. This complicates the solution by classical analytical methods. A widespread way to address this kind of problems is the Finite Element Method (FEM), a numerical approach which solves general differential equations obtaining accurate approximated solutions.

In the FEM, the computational domain is divided into smaller parts, the so-called finite elements. Within each finite element one seeks to approximate the behavior of the variable under study to a simpler function. For instance, referring to a specific body domain, the variable of interest may vary in a highly non-linear manner over it but if the finite elements are small enough, it can be a good approximation to assume that the variable varies in a linear fashion over each element [14]. Thus an approximate solution in the entire computational domain can be obtained.

The Finite Element Method is composed of the following phases [3]:

1. Domain discretization
2. Choice of interpolating function
3. Formulation of the system of ordinary differential equations
4. Solution of the system of equations

In the following sections the first three phases are going to be resumed.

2.1 Space domain discretization

In this work we consider the convective heat transfer problem and we are interested in the temperature distribution within a body that might be composed of different materials. Each with different properties such as thermal conductivity, heat capacity, density, etc.

The whole body domain Ω is divided into *regions*, respecting common materials properties and characteristics. Then, each region is subdivided into elements, geometric entities suited to fill the regions (filling entirely Ω), which cannot intersect.

In the one dimensional case, where the domain is a curve, the elements are line segments (Figure 2.1a), in two dimensions the domain is a surface and the elements are polygons (Figure 2.1b) while in three dimensional case, the domain is a volume and the elements are, for instance, hexahedra or tetrahedra (Figure 2.1c).

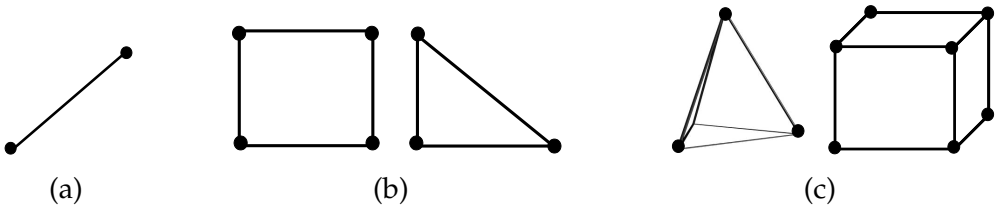

Figure 2.1: Finite Element Samples

The idea behind FEM is to determine the values of the variable under study at certain points (called *nodes*) in each element and find an approximation of the function we are looking for by interpolating between the elements nodes. The nodes are often located at the edges of each element, in Figure 2.1 the nodes are the highlighted points.

2.2 Interpolating functions

The interpolating (or base) functions are an approximation about how the variable changes within each element. Typically these functions are polynomials of any order (linear, quadratic, cubic, etc.). However, it is preferable to choose 1^{st} or 2^{nd} order polynomials, as higher order increase the complexity of the formulation and the computational burden, even though the approximation in the problem description might improve.

Letting T be the unknown analytical solution, the approximation function $T^\star$ in the FEM is made of linear combinations of basis functions ϕ_j defined within each element:

$$T^\star(x, y, z, t) = \sum_{j=1}^{N} \theta_j(t)\ \phi_j(x, y, z), \tag{2.1}$$

where θ_j are the unknown nodal values (N in total) that are to be determined in the solution process.

Each ϕ_j is associated with one node of the FE mesh and it has compact and local support. They are nonzero only over the elements which touch the node they are associated with, i.e. the j-th node, everywhere else they are equal to zero[14]:

$$\phi_j(x_i, y_i, z_i) = 1 \qquad \text{if} \qquad i = j \tag{2.2}$$

$$\phi_j(x_i, y_i, z_i) = 0 \qquad \text{if} \qquad i \neq j \tag{2.3}$$

$$i, j = 1, 2, 3, ..., N. \tag{2.4}$$

Assuming a locally linear behaviour of T within an element, for a the 1-dimensional problem, the approximation functions within a mesh of 5 node are shown in Figure 2.2a. The 2D case is shown instead in Figure 2.2b.

In the present work linear interpolating functions are adopted. As a consequence, $T^\star$ is a piecewise linear function. This remark will be important later, when the weak formulation of the problem is presented.

2.3 Formulation of the problem

2.3.1 Heat equation - Strong form

The temperature distribution is a variable that depends both on time and space, $T = T(x, y, z, t)$. The differential equation associated with thermal conduction is given by the law of conservation of energy and Fouriers law of heat conduction. The resulting equation is:

$$c\rho\frac{\partial T}{\partial t} - \nabla \cdot (\kappa \nabla T) = Q \qquad \text{in} \qquad \Omega \tag{2.5}$$

where T is the continuum temperature, Ω is the problem domain, c [J/kg-K] represents **specific heat**, κ [W/K-m] is the **thermal conductivity**, ρ [kg/m^3]

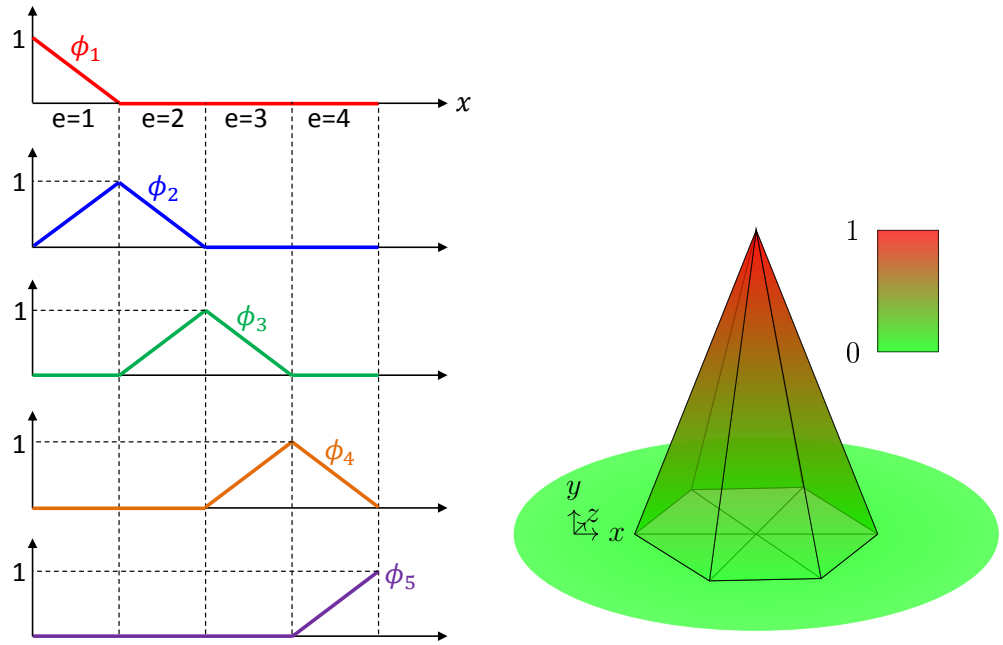

(a) 1-D (b) 2-D

Figure 2.2: Linear interpolating functions

density, of the body materials. Q [W/m^3] represents an external or internal **heat source**. For a complete formulation, boundary conditions have to be specified.

In this work heat transfer boundary conditions are considered. As the bodies under study are assumed to be surrounded by air, there is heat flow between the body and the fluid. To formulate the boundary conditions in the body surface in contact with the air, we refer to the **Newton's cooling law**. Such law states that the rate of heat loss of a body is proportional to the difference in the temperatures between the body and its surroundings:

$$-\kappa \nabla T \cdot \hat{n} = \lambda (T - T_{\text{amb}}), \tag{2.6}$$

being λ the **heat transfer coefficient** [W/m^2-K] and $\hat{n}$ the unit vector at the body boundary, pointing outward.

Eq. 2.5 and 2.6 constitute what is referred as the ***strong form*** of convective heat transfer.

2.3.2 Heat equation - Weak form

The FEM requires the reformulation of the strong form into an integral form called the ***weak form***. There are a number of different ways that can be used to derive the weak form of a differential equation [3]. For the differential equations studied in this work, we exploit to use the **Method of Weighted Residuals (MWR)**. The MWR is based on the idea that the best approximation $T^\star$ of T is the one ensuring the zeroing of the residual:

$$r = c\rho\frac{\partial T^\star}{\partial t} - \kappa\nabla^2 T^\star - Q \tag{2.7}$$

along the problem domain [3].

The MWR minimizes the residuum r in a weighted integral sense:

$$\begin{aligned}\sum_{j=1}^{N}\int_\Omega w_j r\,d\Omega = \sum_{j=1}^{N}\int_\Omega w_j\left(c\rho\frac{\partial T^\star}{\partial t} - \kappa\nabla^2 T^\star - Q\right)d\Omega = \\ = \sum_{j=1}^{N}\int_\Omega w_j c\rho\frac{\partial T^\star}{\partial t}d\Omega - \sum_{j=1}^{N}\int_\Omega w_j\kappa\nabla^2 T^\star d\Omega - \sum_{j=1}^{N}\int_\Omega w_j Q\,d\Omega = 0\end{aligned} \tag{2.8}$$

with test functions $w_j = w_j(x, y, z)$. The MWR finds the solution $T^\star$ that zeros r (in eq. 2.7) by actually solving eq. 2.8.

Due to the choice of linear ϕ_j's, $\nabla^2 T^\star$ can not be evaluated properly since $T^\star$ is piecewise linear. Therefore, the second term of eq. 2.8 needs to be reformulated. Integrating by parts the 2nd term of eq. 2.8, we get:

$$-\sum_{j=1}^{N}\int_\Omega w_j\kappa\nabla^2 T^\star d\Omega = \sum_{j=1}^{N}\int_\Omega \kappa\nabla w_j\nabla T^\star d\Omega - \sum_{j=1}^{N}\int_\Sigma \kappa w_j\nabla T^\star\cdot\hat{n}\,d\Sigma \tag{2.9}$$

The last term of eq. 2.9 is called boundary integral since it is evaluated at the domain boundary (Σ). Notice that its argument coincides with the problem boundary conditions shown in eq. 2.6. Hence, eq. 2.9 can be rewritten as:

$$\sum_{j=1}^{N}\int_\Omega w_j\kappa\nabla^2 T^\star d\Omega = \sum_{j=1}^{N}\int_\Omega \kappa\nabla w_j\nabla T^\star d\Omega + \sum_{j=1}^{N}\int_\Sigma w_j\lambda(T^\star - T_{\text{amb}})d\Sigma \tag{2.10}$$

Finally, substituting eq. 2.10 in 2.8, we get:

$$\sum_{j=1}^{N}\int_{\Omega} w_j c\rho\frac{\partial T^\star}{\partial t}d\Omega + \sum_{j=1}^{N}\int_{\Omega}\kappa\nabla w_j\nabla T^\star d\Omega + \\ -\sum_{j=1}^{N}\int_{\Sigma} w_j\lambda(T^\star - T_{\text{amb}})d\Sigma - \sum_{j=1}^{N}\int_{\Omega} w_j Q d\Omega = 0 \quad (2.11)$$

Eq. 2.11 represents the weak form we were looking for. This form is referred as weak due to its lower differentiability requirements compared to the original weighted residual statement (eq. 2.8). The weak form allows us to work with piecewise linear approximated solutions.

2.3.3 Construction of the approximate solution

We already have all the ingredients needed to construct our solution. Substituting the approximate solution $T^\star$ given in eq. 2.1 into our weak formulation eq. 2.11 we obtain:

$$\sum_{j=1}^{N}\sum_{i=1}^{N}\int_{\Omega} w_j c\rho\phi_i\frac{\partial\theta}{\partial t}d\Omega + \sum_{j=1}^{N}\sum_{i=1}^{N}\int_{\Omega}\kappa\nabla w_j\nabla\phi_i\theta_i d\Omega + \\ +\sum_{j=1}^{N}\sum_{i=1}^{N}\int_{\Sigma} w_j\lambda\phi_i\theta_i d\Sigma = \sum_{j=1}^{N}\int_{\Omega} Q w_j d\Omega + \sum_{j=1}^{N}\int_{\Sigma} w_j\lambda T_{\text{amb}} d\Sigma \quad (2.12)$$

Among the MWR, the most commonly used is the **Galerkin method** in which the test functions w_j are chosen to be equal to the interpolating functions ϕ_j[3]. That is,

$$w_j = \phi_j \qquad \text{for} \qquad j = 1, 2, 3, ..., N \quad (2.13)$$

From this last equation, the following system of ODE is formulated

$$c\rho\boldsymbol{D}\dot{\boldsymbol{\theta}} + (\lambda\boldsymbol{H} + \kappa\boldsymbol{K})\boldsymbol{\theta} = \boldsymbol{q} \quad (2.14)$$

with

$$\boldsymbol{D} = \sum_{j=1}^{N}\sum_{i=1}^{N}\int_{\Omega}\phi_j\phi_i d\Omega \qquad \boldsymbol{K} = \sum_{j=1}^{N}\sum_{i=1}^{N}\int_{\Omega}\nabla\phi_j\nabla\phi_i d\Omega$$

$$\boldsymbol{H} = \sum_{j=1}^{N}\sum_{i=1}^{N}\int_{\Sigma}\phi_j\phi_i d\Sigma$$

$$\boldsymbol{q} = Q\boldsymbol{q}_{\text{in}} + \lambda T_{\text{amb}}\boldsymbol{q}_{\text{conv}} \quad \boldsymbol{q}_{\text{conv}} = \sum_{j=1}^{N}\int_{\Sigma}\phi_j d\Sigma \qquad \boldsymbol{q}_{\text{in}} = \sum_{j=1}^{N}\int_{\Omega}\phi_j d\Omega$$

where $\boldsymbol{\theta} \in \Re^N$ is the vector of nodal unknowns temperatures of the FE mesh. $\boldsymbol{D}$, $\boldsymbol{H}$ and $\boldsymbol{K}$ are $N \times N$ symmetric matrices. The vector $\boldsymbol{q}$ correspond to the excitation/inputs of the thermal model.

In this way the original problem with, in principle, infinitely many unknowns (a continuous distribution), has been replaced by a problem with a finite number of them (N). In general, the more unknowns (a finer spacial discretization), the more accurate the approximate solution but the higher the computational burden.

2.4 Thermal model of an electric machine

An accurate thermal model of the Permanent Magnet Synchronous Motor (PMSM) is crucial in the design of a model based state observer. Starting from the Finite Element Analysis (FEA) explained along the previous section, in this section the thermal model of the PMSM studied in this work is presented.

Experts in FEA from the company NewTwen developed an accurate FE model of the motor that was provided to the author. The real motor, shown in Figure 2.3, is composed of different parts, each made of different materials. The given model is characterized by five domains (Ω_j, $j \in [1,5]$): the rotor (Ω_1) made of aluminum, the stator (Ω_2) made of iron, the winding (Ω_3) made of copper, the printed circuit board (PCB) (Ω_4) made of plastic and the air gap between the rotor and stator (Ω_5). All these domains are depicted in Figure 2.4.

It is worth to mention that for a complete analysis, the physics of fluid dynamics should be considered to model the heat transfer in the air gap in both the stator and rotor. Instead of modelling the air gap as if it were a solid between the rotor and stator with an effective thermal conductivity that captures

both conduction and convection effects. However, the latter was the approach followed in this case since multiphysics simulations involving fluids dynamics have numerical issues, which make the problem difcult to solve [21].

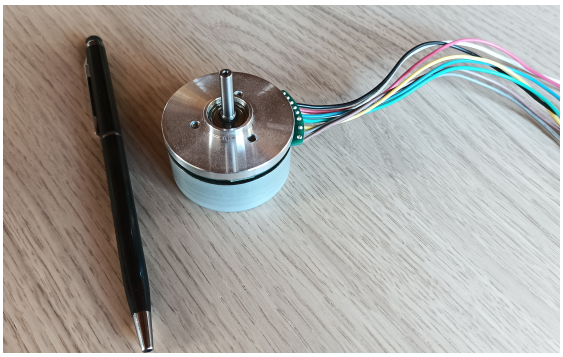

Figure 2.3: PMSM studied

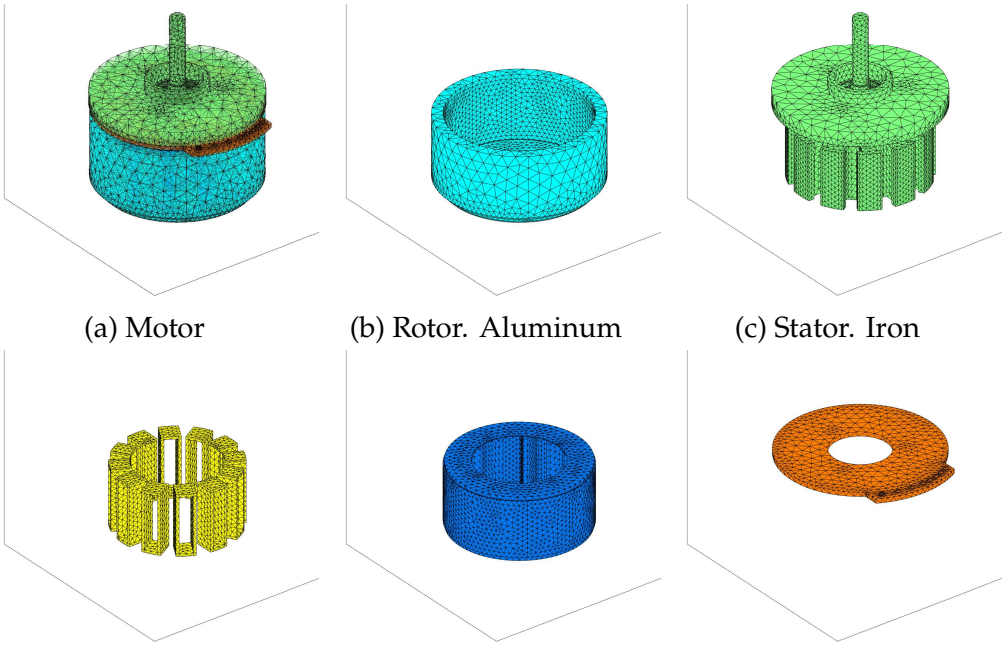

(a) Motor (b) Rotor. Aluminum (c) Stator. Iron

(d) Winding. Copper (e) Air gap. Air (f) PCB

Figure 2.4: Motor domains

For this system with five domains, the system of ODE presented in eq. 2.14 becomes:

$$\boldsymbol{D}_{\mathrm{M}}\dot{\boldsymbol{\theta}} + (\boldsymbol{H}_{\mathrm{M}} + \boldsymbol{K}_{\mathrm{M}})\boldsymbol{\theta} = \boldsymbol{q}_{\mathrm{M}} \tag{2.15}$$

where the matrices $\boldsymbol{D}_{\mathrm{M}}$, $\boldsymbol{K}_{\mathrm{M}}$, $\boldsymbol{H}_{\mathrm{M}}$ and the vector $\boldsymbol{q}_{\mathrm{M}}$ are defined as:

$$
\begin{aligned}
&\boldsymbol{D}_{\mathrm{M}} = \sum_{l=1}^{5} \rho_l c_l \boldsymbol{D_l} && c_l,\ \rho_l \text{ specific heat and density of } l^{\text{th}} \text{ material} \\
&\boldsymbol{K}_{\mathrm{M}} = \sum_{l=1}^{5} \kappa_l \boldsymbol{H_l} && k \text{ thermal conductivity of } l^{\text{th}} \text{ material} \\
&\boldsymbol{H}_{\mathrm{M}} = \lambda \boldsymbol{H} && \\
&\boldsymbol{D_l} = \sum_{j=1}^{N} \sum_{i=1}^{N} \int_{\Omega_l} \phi_j \phi_i d\Omega_l && \text{for } l = 1, 2, 3, 4, 5 \\
&\boldsymbol{K_l} = \sum_{j=1}^{N} \sum_{i=1}^{N} \int_{\Omega_l} \nabla\phi_j \nabla\phi_i d\Omega_l && \\
&\boldsymbol{q}_{\mathrm{M}} = \alpha I^2 \boldsymbol{q}_{\mathrm{in}} + \lambda T_{\mathrm{amb}} \boldsymbol{q}_{\mathrm{conv}} && \alpha = 1 + 0.004(T_{\mathrm{Cu}} - T_{\mathrm{amb}})
\end{aligned}
\tag{2.16}
$$

In the definition of $\boldsymbol{q}_{\mathrm{M}}$, I is the current that flows through the stator winding and α is the copper electrical resistivity, that depends linearly on the temperature of the copper (T_{Cu}).

Due to the complex geometry of the motor, and the size of the finite elements (tetrahedra of size in the order of mm), the system of equations 2.15 has thousands of nodal temperatures to be found. Solving such a system by conventional simulation methods is very time-consuming. To perform simulations in a reasonable time, as well as being able to perform the model calibration and posterior validation, Model Order Reduction (MOR) techniques were implemented by the developers of the motor model.

MOR is a popular method to overcome the computational demand required to solve high dimensional problems. By MOR, a small dimensional approximated system can be derived, from a complex high fidelity one, so that it can reliably replace the original system during the simulation [2]. More specifically, what it was done was a Parametric Model Order Reduction (PMOR), whose main goal is to preserve parameters in the system as symbolic quantities in the reduced-order model. Thus, a change in parameters does not require to perform again the order reduction, but simply the evaluation of the reduced-order model for the new parameter values[2].

The most common approach to obtain a reduced-order model of a system as

the one in eq. 2.15 is via projection, i.e., by projecting the dynamics of full-order model (of dimension N) on a lower-dimensional subspace (of dimension d), where $d \ll N$. This is followed by re-projecting the reduced dynamics onto the original space to obtain the approximation. The approach followed by the model designers is similar to what is explained in [2] and [19], where readers may find further information. Once the model was reduced, calibrated and validated, the results were provided to the author of this work to design the desired observer.

Since the reduced order model and the original one share the same parameters and structure but different dimension, from now on there will be no distinctions between them.

Even though the motor model dimension was reduced, the motor geometry and properties makes complex the design of a robust temperature observer. In view of this, in the present work it is proposed the study of the one dimensional heat transfer problem by using as a system a metal bar model.

2.5 Thermal model of a metal bar

Our reference system is an aluminum bar of rectangular cross section. Starting from the general 3-D formulation carried out is section 2.3, we will focus on the study of one dimensional convective heat transfer. Specifically, we are interested in how the temperature changes over time after a heat source has been placed on one side of the bar, before and after the steady state situation has been reached.

In reality one cannot think of a one-dimensional heat transfer problem, but we could assume that the thickness of the bar is small in relation to its length so that temperature variations along the bar axis are much larger than transversal variations. Moreover, it is assumed that the rod is sufficiently thin so that the temperature within any particular cross-section is constant. As an example, Figure 2.5 shows a graphic representation of the bar discretised by $N = 10$ nodes and $m = 9$ elements.

The system of ODEs for this body has exactly the same structure presented in eq. 2.14, consisting of $N = 10$ unknowns and only 4 parameters ρ, c, λ and k. In fact, we are working with only one material, aluminum.

In this case everything is one dimensional and we choose linear shape functions (as those of Figure 2.2a).

As it is depicted in Figure 2.6, the element e_4 goes from node n_4 to n_5 and the

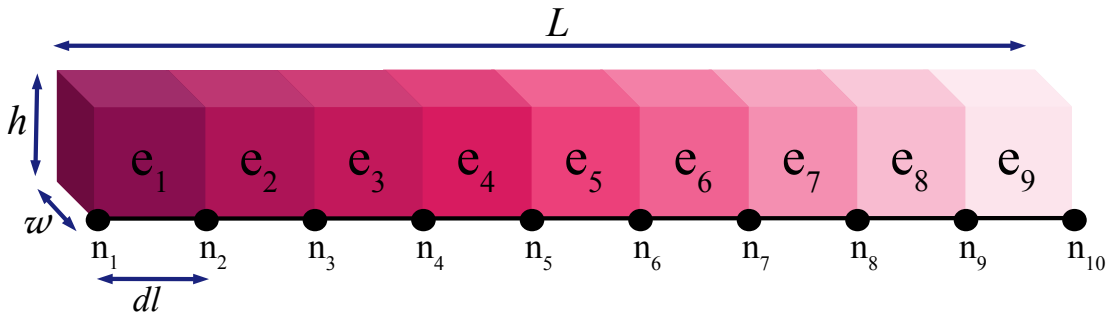

Figure 2.5: Graphic representation of aluminum bar with thermal source at left side

element e_4 goes from node n_5 to n_6. Two consecutive elements have one node in common.

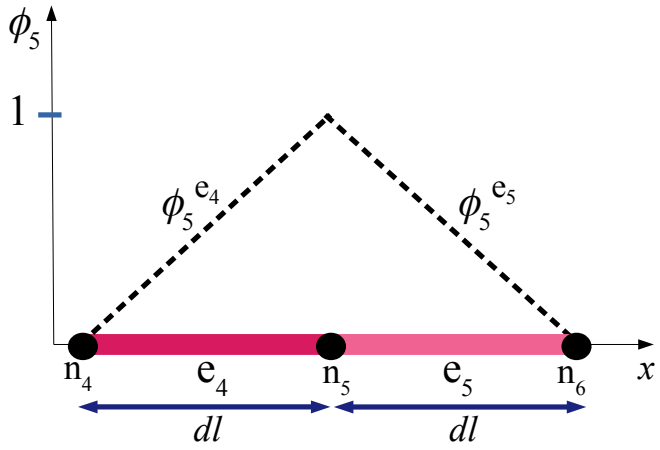

Figure 2.6: 1D interpolating function for the aluminum bar

Then, the corresponding shape functions associated to node n_5 are:

$$\phi_5^{e_4} = \frac{x}{dl} \quad , \quad (x \in e_4)$$
$$\phi_5^{e_5} = 1 - \frac{x}{dl} \quad , \quad (x \in e_5)$$

hence

$$\phi_5 = \phi_5^{e_4} + \phi_5^{e_5}$$

the superscripts e_4 and e_5 denotes that these shape functions are for local elements and the subscript 5 denotes the node they are associated with.

Therefore, for two consecutive elements having node i in common:

$$\phi_{=}\phi_i^{\mathrm{e}_k} + \phi_i^{\mathrm{e}_{k+1}} \tag{2.17}$$

With the basis functions defined, the system of ODEs characterizing the aluminum bar thermal behavior is given by:

$$c\rho \boldsymbol{D}_{\mathrm{B}}\dot{\boldsymbol{\theta}}_{\mathrm{B}} + (\lambda \boldsymbol{H}_{\mathrm{B}} + \kappa \boldsymbol{K}_{\mathrm{B}})\boldsymbol{\theta}_{\mathrm{B}} = \boldsymbol{q}_{\mathrm{B}} \tag{2.18}$$

with

$$\boldsymbol{D}_{\mathrm{B}} = \sum_{j=1}^{N}\sum_{i=1}^{N}\int_0^L \phi_j\phi_i hwdl \qquad \boldsymbol{K}_{\mathrm{B}} = \sum_{j=1}^{N}\sum_{i=1}^{N}\int_0^L \nabla\phi_j\nabla\phi_i hwdl$$

$$\boldsymbol{H}_{\mathrm{B}} = \sum_{j=1}^{N}\sum_{i=1}^{N}\int_0^L \phi_j\phi_i(2w+2h)dl$$

$$\boldsymbol{q}_{\mathrm{conv}} = \sum_{j=1}^{N}\int_0^L \phi_j(2w+2h)dl \qquad \boldsymbol{q}_{\mathrm{in}} = \sum_{j=1}^{N}\int_0^L \phi_j hwdl$$

$$\boldsymbol{q}_{\mathrm{B}} = Q\boldsymbol{q}_{\mathrm{in}} + \lambda T_{\mathrm{amb}}\boldsymbol{q}_{\mathrm{conv}}$$

The models obtained in eqs. 2.18 and is the model required to start with the design of our robust model-based temperature estimator.

2.6 Models time discretization

The *discretization problem* consists of finding a discrete-time system of equations (Ordinary Difference Equations) such that its solution approximates the solution of the continuous-time system.

Starting from a continuous-time system, Υ_{CT}, formulated in state-space

$$\Upsilon_{\mathrm{CT}} = \begin{cases} \dot{\boldsymbol{x}}(t) = \boldsymbol{\Phi}\boldsymbol{x}(t) + \boldsymbol{\Gamma}\boldsymbol{u}(t) \\ \boldsymbol{y}(t) = \boldsymbol{\Psi}\boldsymbol{x}(t) + \boldsymbol{\Omega}\boldsymbol{u}(t) \end{cases} \tag{2.19}$$

the state evolution equation

$$\dot{\boldsymbol{x}}(t) = \boldsymbol{\Phi}\boldsymbol{x}(t) + \boldsymbol{\Gamma}\boldsymbol{u}(t)$$

can be integrated to yield different representation of the system matrices $\mathbf{\Phi}$, $\mathbf{\Gamma}$, $\mathbf{\Psi}$ and $\mathbf{\Omega}$, depending on the discretization method used.

In Table 2.1 are summarized the formulas which directly relate the state-space matrices of the continuous-time model to those of the discrete-time counterpart. The sampling period is identified as T_s. In this table are presented the results of using Backward and Forward Euler as well as the *Exact* discretization method. The formers are based on the Euler's integration methods. The later is based on the implementation of an Analog to Digital Converter and a Zero-Order Holder at the output and input of the plant respectively to convert it into a sampled data system. This approach is explained in details in [7].

It is important to mention that in order to capture the system dynamics, T_s has to be chosen respecting the system characteristics modes. However, when using the Forward Euler method special attention has to be payed since a wrong choice of T_s can lead to instabilities of the discretized system. A T_s suitable for a system discretized with Backward Euler can be inappropriate (too large) for the same system but discretized with Forward Euler method.

	Forward Euler	Backward Euler	Exact
$\boldsymbol{A}$	$\mathbb{I} - \mathbf{\Phi} T_s$	$(\mathbb{I} - \mathbf{\Phi} T_s)^{-1}$	$\boldsymbol{e}^{\mathbf{\Phi} T_s}$
$\boldsymbol{B}$	$T_s \mathbf{\Gamma}$	$(\mathbb{I} - \mathbf{\Phi} T_s)^{-1} T_s \mathbf{\Gamma}$	$\int_0^{T_s} \boldsymbol{e}^{\mathbf{\Phi} T_s} \mathbf{\Gamma} d\tau$
$\boldsymbol{C}$	$\mathbf{\Psi}$	$\mathbf{\Psi}(\mathbb{I} - \mathbf{\Phi} T_s)^{-1}$	$\mathbf{\Psi}$
$\boldsymbol{J}$	$\mathbf{\Omega}$	$\mathbf{\Omega} + \mathbf{\Psi}(\mathbb{I} - \mathbf{\Phi} T_s)^{-1} T_s \mathbf{\Gamma}$	$\mathbf{\Omega}$

Table 2.1: Discretization of a continuoustime statespace model $\Upsilon_c = (\mathbf{\Phi}, \mathbf{\Gamma}, \mathbf{\Psi}, \mathbf{\Omega})$

3

Kalman Filter

As it was mentioned in chapter 1, the main interest of this research project is to design a model-based temperature observer capable of estimating temperatures at many different points of a Permanent Magnet Synchronous Motor (PMSM). With the help of only few sensors placed on the machine, the estimator needs to be robust enough to overcome mild model mismatches, uncertainties in model parameters and uncontrolled system inputs.

A state observer is a dynamical system that provides an estimate of the state vector based on the available data: the system outputs (sensor measurements) and inputs, as it is shown in Figure 3.1.

The top branch of the diagram in Figure 3.1 shows the operation of the physical system (denoted by "true system"). In our case, the actual PMSM. The input to the PMSM ($\boldsymbol{u}_k$) is the electrical current that it experiences and the temperature of the external environment. The output ($\boldsymbol{y}_k$) is the temperature at accessible points where thermal sensors are placed. Inside the PMSM there are some points where a thermal sensors cannot be placed (or is not desired), i.e. those temperatures cannot be measurable. In those inaccessible points is where the temperature has to be estimated.

The bottom branch of Figure 3.1 shows the operation of the state estimator. It is based on a model of the physical system and an algorithm that drives the state estimates $\hat{\boldsymbol{x}}_k$ towards the actual states $\boldsymbol{x}_k$.

Kalman filtering provides an elegant and powerful solution as far as state estimation is concerned. The Kalman filter (KF) is the optimum method to estimate the unmeasured state $\boldsymbol{x}_k$ of the corresponding physical system, in real

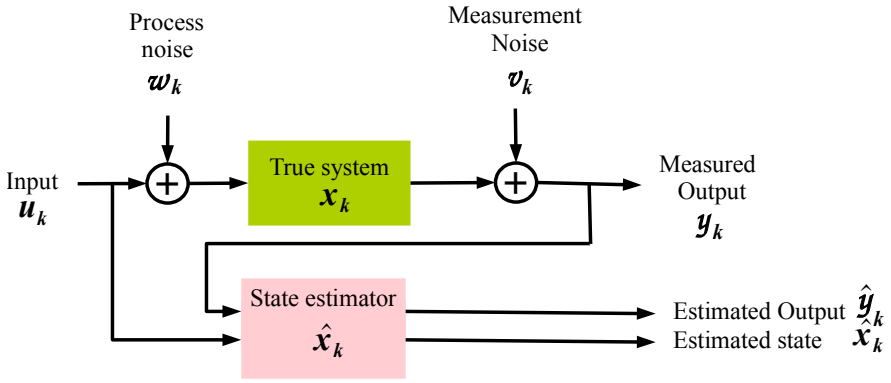

Figure 3.1: The model-based estimation approach

time, in a dynamic environment, given knowledge of the system´s measured input/output signals. The KF comprises a set of recursive equations that are repeatedly evaluated as the physical system operates [18].

We will not directly derive these equations here, rather the following discussion will be directed to their introduction and practical implementation. The reader is referred to Kalman`s original paper [9] and related textbooks like [17] and [4] for further derivation details.

3.1 Linear Kalman Filter

For the design of the linear KF we will assume that the physical system under study can be modeled as linear time invariant system represented in the following system of difference equations in its state-space form,

$$\Upsilon: \begin{cases} \boldsymbol{x}_{k+1} = \boldsymbol{A}\boldsymbol{x}_k + \boldsymbol{B}\boldsymbol{u}_k + \boldsymbol{w}_k \\ \boldsymbol{y}_k = \boldsymbol{C}\boldsymbol{x}_k + \boldsymbol{v}_k \end{cases} \tag{3.1}$$

where $\boldsymbol{x}_k \in \Re^n$ is the system state vector at time index k. The known/deterministic input to the system is $\boldsymbol{u}_k \in \Re^p$, and $\boldsymbol{w}_k \in \Re^n$ is stochastic "process noise" or "disturbance" that models some unmeasured input which affects the state of the system [18]. The output of the system $\boldsymbol{y}_k \in \Re^m$, is computed as a linear combination of states and input plus $\boldsymbol{v}_k \in \Re^m$, which models "sensor noise" that affects the measurement of the system output but does not affect the system state [18]. The matrices $\boldsymbol{A} \in \Re^{n\times n}$, $\boldsymbol{B} \in \Re^{n\times p}$, $\boldsymbol{C} \in \Re^{m\times n}$ describe the dynamics of the system.

Certain assumptions are made when deriving the KF equations. First of

all, both $\boldsymbol{w}_k$ and $\boldsymbol{v}_k$ are assumed to be mutually uncorrelated white Gaussian random processes, with zero mean and covariance matrices $\boldsymbol{Q}_w = \boldsymbol{Q}_w^{\mathrm{T}} \geq 0$ and $\boldsymbol{R}_v = \boldsymbol{R}_v^{\mathrm{T}} > 0$ with known value:

$$\mathbb{E}\left[\boldsymbol{w}_s \boldsymbol{w}_k^{\mathrm{T}}\right] = \begin{cases} \boldsymbol{Q}_w & s = k \\ 0 & s \neq k \end{cases}; \qquad \mathbb{E}\left[\boldsymbol{v}_s \boldsymbol{v}_k^{\mathrm{T}}\right] = \begin{cases} \boldsymbol{R}_v & s = k \\ 0 & s \neq k \end{cases} \tag{3.2}$$

and $\mathbb{E}\left[\boldsymbol{w}_k \boldsymbol{x}_0^{\mathrm{T}}\right] = 0 \quad \forall \quad k > 0$, where $\boldsymbol{x}_0$ is the state initial condition. The assumptions on the noise processes $\boldsymbol{w}_k$ and $\boldsymbol{v}_k$ are rarely (never) met in practice, but the consensus of the literature is that the method still works very well [18], [4].

The KF goal is to find the minimum mean squared error estimate $\hat{\boldsymbol{x}}_k$ of the true state $\boldsymbol{x}_k$, using the input/output data $\{\boldsymbol{u}_0, \boldsymbol{u}_1, \ldots, \boldsymbol{u}_k\}$, $\{\boldsymbol{y}_0, \boldsymbol{y}_1, \ldots, \boldsymbol{y}_k\}$, the physical system model (eq. 3.1), and the assumptions on $\boldsymbol{w}_k$ and $\boldsymbol{v}_k$. The KF algorithm is a set of recursive operations that returns, at each iteration, an estimate of the state itself, and also the covariance matrix $\boldsymbol{\Sigma}_{\tilde{\boldsymbol{x}},k} = \mathbb{E}\left[\tilde{\boldsymbol{x}}_k \tilde{\boldsymbol{x}}_k^{\mathrm{T}}\right]$ of the state estimate error $\tilde{\boldsymbol{x}}_k = \boldsymbol{x}_k - \hat{\boldsymbol{x}}_k$. The covariance matrix $\boldsymbol{\Sigma}_{\tilde{\boldsymbol{x}},k}^{+}$indicates the uncertainty of the state estimate $\hat{\boldsymbol{x}}_k^{+}$. A summary of the KF solution is presented in Algorithm 1.

During each sampling interval, before any system measurements are made, the *prediction* phase is carried out. The discrete-time KF computes the prediction of the state $\hat{\boldsymbol{x}}_k^{-}$ and the error covariance matrix $\boldsymbol{\Sigma}_{\tilde{\boldsymbol{x}},k}^{-}$; based on the estimate obtained in the previous iteration, $\hat{\boldsymbol{x}}_{k-1}^{+}$, and the model system dynamics (eq. 3.1). Later, after measuring the system output $\boldsymbol{y}_k$, comes the *update* phase. The predictions $\hat{\boldsymbol{x}}_k^{-}$ and $\boldsymbol{\Sigma}_{\tilde{\boldsymbol{x}},k}^{-}$ are updated, based on the new information just arrived. Then, it is obtained the state estimate we are looking for, $\hat{\boldsymbol{x}}_k^{+}$ and the corresponding error covariance matrix $\boldsymbol{\Sigma}_{\tilde{\boldsymbol{x}},k}^{+}$. $\hat{\boldsymbol{x}}_k^{+}$ and $\boldsymbol{\Sigma}_{\tilde{\boldsymbol{x}},k}^{+}$ are then more accurate than $\hat{\boldsymbol{x}}_k^{-}$ and $\boldsymbol{\Sigma}_{\tilde{\boldsymbol{x}},k}^{-}$ as they incorporate knowledge gleaned from the measurement $\boldsymbol{y}_k$.

The information that comes with each measurement is represented in the difference between the sensor measurement $\boldsymbol{y}_k$ and the predicted one $\hat{\boldsymbol{y}}_k$, called the *innovation* $\boldsymbol{e}_k$. $\boldsymbol{e}_k$ may be nonzero due to measurement noise, an incorrect state prediction $\hat{\boldsymbol{x}}_k^{-}$, or an inaccurate model. We see in Algorithm 1, that the *Kalman gain* vector $\boldsymbol{L}_k$ multiplies the innovation when calculating the state-estimate update, $\boldsymbol{L}_k \boldsymbol{e}_k$. How large or small is this update depends on a series of considerations:

Algorithm 1 Linear Kalman filter summary [18]

Initialization:
  for $k = 0$ **do**
    $\hat{\boldsymbol{x}}_0^+ = \mathbb{E}[\boldsymbol{x}_0]$
    $\boldsymbol{\Sigma}_{\tilde{\boldsymbol{x}},0}^+ = \mathbb{E}\left[(\boldsymbol{x}_0 - \hat{\boldsymbol{x}}_0^+)(\boldsymbol{x}_0 - \hat{\boldsymbol{x}}_0^+)^{\mathrm{T}}\right]$
  end for
Computation:
  for $k = 1, 2, \ldots$ **do**
    {**PREDICTION**}
    State estimate time update:
      $\hat{\boldsymbol{x}}_{k+1}^- = \boldsymbol{A}\hat{\boldsymbol{x}}_k^+ + \boldsymbol{B}\boldsymbol{u}_k$
    Error covariance time update:
      $\boldsymbol{\Sigma}_{\tilde{\boldsymbol{x}},k+1}^- = \boldsymbol{A}\boldsymbol{\Sigma}_{\tilde{\boldsymbol{x}},k}^+\boldsymbol{A}^{\mathrm{T}} + \boldsymbol{Q}_w$
    Kalman gain matrix calculation:
      $\boldsymbol{L}_{k+1} = \boldsymbol{\Sigma}_{\tilde{\boldsymbol{x}},k+1}^-\boldsymbol{C}^{\mathrm{T}}\left[\boldsymbol{C}\boldsymbol{\Sigma}_{\tilde{\boldsymbol{x}},k+1}^-\boldsymbol{C}^{\mathrm{T}} + \boldsymbol{R}_v\right]^{-1}$
    Innovation calculation:
      $\boldsymbol{e}_{k+1} = \boldsymbol{y}_{k+1} - \hat{\boldsymbol{y}}_{k+1} = \boldsymbol{y}_{k+1} - \boldsymbol{C}\hat{\boldsymbol{x}}_{k+1}^-$
    {**UPDATE**}
    State estimate measurement update:
      $\hat{\boldsymbol{x}}_{k+1}^+ = \hat{\boldsymbol{x}}_{k+1}^- + \boldsymbol{L}_{k+1}\boldsymbol{e}_{k+1}$
    Error covariance measurement update:
      $\boldsymbol{\Sigma}_{\tilde{\boldsymbol{x}},k+1}^+ = (\mathbb{I} - \boldsymbol{L}_{k+1}\boldsymbol{C})\boldsymbol{\Sigma}_{\tilde{\boldsymbol{x}},k+1}^-$
  end for

- The state-estimate update is directly proportional to $\boldsymbol{e}_k$, the larger (smaller) $\boldsymbol{e}_k$ the larger (smaller) tends to be the update;
- If $\hat{\boldsymbol{x}}_k^-$ is very uncertain ($\boldsymbol{\Sigma}_{\tilde{\boldsymbol{x}},k}^-$ is "large"), the values in $\boldsymbol{L}_k$ tend to be large, forcing a large state-estimate update;
- If $\hat{\boldsymbol{x}}_k^-$ is certain ($\boldsymbol{\Sigma}_{\tilde{\boldsymbol{x}},k}^-$ is "small"), the values in $\boldsymbol{L}_k$ tend to be small, reducing the state-estimate update;
- If $\boldsymbol{R}_v$ is large (large sensor noise), the values in $\boldsymbol{L}_k$ tends to be small, reducing the state-estimate update.

A covariance matrix is "large" ("small") the larger (smaller) its singular values are.

3.1.1 Kalman Filter as a dynamical system

With the intuition developed in the previous section, it is clear that the KF is a (synthetic) dynamical system, $\hat{\Upsilon}$, that evolves in time and whose inputs are the

measured (sampled) inputs and outputs of the physical system. In this section we will talk about the characteristics of $\hat{\Upsilon}$ and how they are related to those of the physical system model Υ.

Starting from Υ: $[\boldsymbol{A}, \boldsymbol{B}, \boldsymbol{C}, \boldsymbol{0}]$ (eq. 3.1) and the assumptions done about process and sensor noises (eq. 3.2), $\hat{\Upsilon}$ is a closed loop system with the following dynamical model:

$$\hat{\Upsilon}: \begin{cases} \hat{\boldsymbol{x}}_{k+1}^{+} = (\mathbb{I} - \boldsymbol{L}_k \boldsymbol{C})\boldsymbol{A}\hat{\boldsymbol{x}}_k^{+} + (\mathbb{I} - \boldsymbol{L}_k \boldsymbol{C})\boldsymbol{B}\boldsymbol{u}_k + \boldsymbol{L}_k \boldsymbol{y}_k \\ \hat{\boldsymbol{y}}_k = \boldsymbol{C}\hat{\boldsymbol{x}}_k^{+} \end{cases} \tag{3.3}$$

considering $\boldsymbol{D}_k = \boldsymbol{0}$ for both $\hat{\Upsilon}$ and Υ, for simplicity.

In order to design a suitable KF it is necessary to verify that it has the following features. The filter has to be simultaneously time invariant, or at least asymptotically time invariant, and asymptotically stable [1].

The time invariance, or asymptotic time invariance, arises when for any nonnegative symmetric initial condition $\boldsymbol{\Sigma}_{\tilde{\boldsymbol{x}},0}$, one has a constant error covariance as time tends to infinity, i.e.

$$\lim_{k \to \infty} \boldsymbol{\Sigma}_{\tilde{\boldsymbol{x}},k} = \bar{\boldsymbol{\Sigma}} \tag{3.4}$$

and $\bar{\boldsymbol{\Sigma}}$ is the unique symmetric positive semidefinite solution of the discrete algebraic Riccati equation [1]. With $\bar{\boldsymbol{\Sigma}}$ a constant, the Kalman gain $\boldsymbol{L}_k$ tends to a constant value $\bar{\boldsymbol{L}}$.

The asymptotic stability of $\hat{\Upsilon}$ is guaranteed if all its eigenvalues are inside the unitary circle. That is,

$$|\sigma(\boldsymbol{A} - \bar{\boldsymbol{L}}\boldsymbol{C}\boldsymbol{A})| < 1 \tag{3.5}$$

The $\hat{\Upsilon}$ is provided with these two key features if the system Υ (eq. 3.1) is both detectable and stabilizable [1].

Observing the dynamics of $\tilde{\boldsymbol{x}}_k$:

$$\tilde{\boldsymbol{x}}_{k+1} = (\mathbb{I} - \boldsymbol{L}_k \boldsymbol{C})\boldsymbol{A}\tilde{\boldsymbol{x}}_k + (\mathbb{I} - \boldsymbol{L}_k \boldsymbol{C})\boldsymbol{w}_k - \boldsymbol{L}_k \boldsymbol{v}_k \tag{3.6}$$

it converges asymptotically to zero, what is desired from an asymptotic observer, if the asymptotic stability of $\hat{\Upsilon}$ is met.

3.2 Offset-free Linear Kalman filter

The performance of the KF is related to the model accuracy. The KF approach takes into account model mismatches with the inclusion of the process noise $\boldsymbol{w}_k$. However, in practice, modeling error and unmeasured disturbances can lead to steady-state offset, overall when the assumptions 3.2 are not met, which occurs in most cases.

An approach to eliminating steady-state offset involves augmenting the process model to include a constant step disturbance [16]. The knowledge of the physical system might suggest the presence of such unmeasured disturbance, but the inclusion of such an unmeasured disturbance in the physical system model could also be a convenient way to account for a model-plant mismatch.

Let's think of a new plant model, Υ', in which the model mismatches are unknown additive quantities affecting the nominal values of the dynamical model matrices $\boldsymbol{A}$ and $\boldsymbol{B}$.

$$\Upsilon': \begin{cases} \boldsymbol{x}_{k+1} = (\boldsymbol{A} + \Delta\boldsymbol{A})\boldsymbol{x}_k + (\boldsymbol{B} + \Delta\boldsymbol{B})\boldsymbol{u}_k + \boldsymbol{w}_k \\ \boldsymbol{y}_k = \boldsymbol{C}\boldsymbol{x}_k + \boldsymbol{v}_k \end{cases} \tag{3.7}$$

Now, let's think of designing a KF starting from such a model with unknown quantities $\Delta\boldsymbol{A}$ and $\Delta\boldsymbol{B}$. The error dynamics would be the one modeled in the following way:

$$\begin{aligned} \tilde{\boldsymbol{x}}_{k+1} = (\mathbb{I} - \boldsymbol{L}_k\boldsymbol{C})\boldsymbol{A}\tilde{\boldsymbol{x}}_k + (\mathbb{I} - \boldsymbol{L}_k\boldsymbol{C})\boldsymbol{w}_k - \boldsymbol{L}_k\boldsymbol{v}_k + \\ + (\mathbb{I} - \boldsymbol{L}_k\boldsymbol{C})\Delta\boldsymbol{A}\boldsymbol{x}_k + (\mathbb{I} - \boldsymbol{L}_k\boldsymbol{C})\Delta\boldsymbol{B}\boldsymbol{u}_k \end{aligned} \tag{3.8}$$

it is appreciated that the asymptotic stability of $\tilde{\boldsymbol{x}}_k$ is not guaranteed, due to the addition of two term which are function of $\boldsymbol{x}_k$ and $\boldsymbol{u}_k$. In steady state, when the input, the state and the Kalman gain become constants, $\boldsymbol{u}_\infty$, $\boldsymbol{x}_\infty$ and $\boldsymbol{L}_\infty$ respectively, there will exist a nonzero offset given by,

$$a = (\mathbb{I} - \boldsymbol{L}_\infty\boldsymbol{C})\Delta\boldsymbol{A}\boldsymbol{x}_\infty + (\mathbb{I} - \boldsymbol{L}_\infty\boldsymbol{C})\Delta\boldsymbol{B}\boldsymbol{u}_\infty \tag{3.9}$$

which will be equal to zero only if $\boldsymbol{x}_\infty \in \mathrm{Ker}((\mathbb{I} - \boldsymbol{L}_\infty\boldsymbol{C})\Delta\boldsymbol{A})$ and $\boldsymbol{u}_\infty \in \mathrm{Ker}((\mathbb{I} - \boldsymbol{L}_\infty\boldsymbol{C})\Delta\boldsymbol{B})$, a very special and almost improbable case.

The appearance of this steady-state offset motivated us to use one of the approaches commonly used in Model Predictive Control to design offset-free

controllers, as in [16], [12] and [15]. In order to remove steady-state error, this approach contemplates the design of a model, starting from the original system, which includes a replicate of the constant nonzero disturbance model, resulting in a new model with augmented state. The augmentation of Υ (eq. 3.1) results in the following system model:

$$\Upsilon_{\text{aug}}: \begin{cases} \begin{bmatrix} \boldsymbol{x}_{k+1} \\ \boldsymbol{d}_{k+1} \end{bmatrix} = \begin{bmatrix} \boldsymbol{A} & \boldsymbol{B}_d \\ \boldsymbol{0}_{n_d \times n} & \mathbb{I}_{n_d \times n_d} \end{bmatrix} \begin{bmatrix} \boldsymbol{x}_k \\ \boldsymbol{d}_k \end{bmatrix} + \begin{bmatrix} \boldsymbol{B} \\ \boldsymbol{0}_{n_d \times p} \end{bmatrix} \boldsymbol{u}_k + \boldsymbol{w}_{\text{a},k} \\ \boldsymbol{y}_k = \begin{bmatrix} \boldsymbol{C} & \boldsymbol{C}_d \end{bmatrix} \begin{bmatrix} \boldsymbol{x}_k \\ \boldsymbol{d}_k \end{bmatrix} + \boldsymbol{v}_{\text{a},k} \end{cases} \tag{3.10}$$

with $\boldsymbol{d}_k \in \mathfrak{R}^{n_d}$, $\boldsymbol{B}_d \in \mathfrak{R}^{n \times n_d}$ and $\boldsymbol{C}_d \in \mathfrak{R}^{m \times n_d}$. The process and sensor noises $\boldsymbol{w}_{\text{a},k} \in \mathfrak{R}^{n+n_d}$ and $\boldsymbol{v}_{\text{a},k} \in \mathfrak{R}^{p}$ meet the conditions set out in 3.2 with covariance matrices $\boldsymbol{Q}_{\text{a},w} \in \mathfrak{R}^{(n+n_d)\times(n+n_d)}$ symmetric positive semidefinite and $\boldsymbol{R}_{\text{a},v} \in \mathfrak{R}^{p \times p}$ symmetric positive definite, respectively. $\boldsymbol{B}_d$ and $\boldsymbol{C}_d$ determine the effect of the disturbance on the states and the output of the system.

In a more general way, with a state variable $\boldsymbol{z}_k = \begin{bmatrix} \boldsymbol{x}_k \\ \boldsymbol{d}_k \end{bmatrix}$, Υ_{aug} can be written as follows:

$$\Upsilon_{\text{aug}}: \begin{cases} \boldsymbol{z}_{k+1} = \boldsymbol{A}_{\text{a}} \boldsymbol{z}_k + \boldsymbol{B}_{\text{a}} \boldsymbol{u}_k + \boldsymbol{w}_{\text{a},k} \\ \boldsymbol{y}_k = \boldsymbol{C}_{\text{a}} \boldsymbol{z}_k + \boldsymbol{v}_k \end{cases} \tag{3.11}$$

Since $\boldsymbol{d}_k$ is assumed to remain constant, it is inherently not asymptotically stable. Hence, this portion of the augmented state needs to be necessarily observable.In other words, if $(\boldsymbol{A}_{\text{a}}, \boldsymbol{B}_{\text{a}})$ is not fully observable, it has to be at least detectable, with non observable states different from $\boldsymbol{d}_k$. Otherwise, the design of an asymptotic state observer is meaningless. Authors in [15] present the main results regarding the detectability of augmented system models as Υ_{aug}:

1. The pair $(\boldsymbol{A}_{\text{a}}, \boldsymbol{B}_{\text{a}})$ (eq. 3.11) is detectable (observable) if and only if the pair $(\boldsymbol{A}, \boldsymbol{C})$ (eq 3.1) is detectable (observable) and

$$\text{rank} \begin{bmatrix} (\mathbb{I} - \boldsymbol{A}) & -\boldsymbol{B}_d \\ \boldsymbol{C} & \boldsymbol{C}_d \end{bmatrix} = n + n_d \tag{3.12}$$

2. There exist matrices $(\boldsymbol{B}_d, \boldsymbol{C}_d)$ such that condition 3.12 holds if and only if the number of outputs is greater than or equal to the number state disturbances $(n_d \leq p)$.

Referring to Υ_{aug}, $\boldsymbol{z}_k$ can be estimated from $\boldsymbol{y}_k$ by using a KF designed for

Υ_{aug}, as it was explained in section 3.1. Thus, $\boldsymbol{x}_k$ and $\boldsymbol{d}_k$ are estimated as follows,

$$\hat{\boldsymbol{z}}_{k+1}^{+} = \begin{bmatrix} \hat{\boldsymbol{x}}_{k+1}^{+} \\ \hat{\boldsymbol{d}}_{k+1}^{+} \end{bmatrix} = (\mathbb{I} - \boldsymbol{L}_{\text{a},k}\boldsymbol{C}_{\text{a}})\boldsymbol{A}_{\text{a}}\hat{\boldsymbol{z}}_{k}^{+} + (\mathbb{I} - \boldsymbol{L}_{\text{a},k}\boldsymbol{C}_{\text{a}})\boldsymbol{B}_{\text{a}}\boldsymbol{u}_k + \boldsymbol{L}_{\text{a},k}\boldsymbol{y}_k \tag{3.13}$$

We remind that the asymtoptic that asymptotic stability of the Υ_{aug} is ensured if the eigenvalues of the matrix $(\mathbb{I} - \boldsymbol{L}_{\text{a},k}\boldsymbol{C}_{\text{a}})\boldsymbol{A}_{\text{a}}$ are all stable. Stability of the augmented system, guarantees asymptotic stability of the estimation error $\tilde{\boldsymbol{z}}_k$, as it can be noticed

$$\tilde{\boldsymbol{z}}_{k+1} = (\mathbb{I} - \boldsymbol{L}_{\text{a},k}\boldsymbol{C}_{\text{a}})\boldsymbol{A}_{\text{a}}\tilde{\boldsymbol{z}}_k + (\mathbb{I} - \boldsymbol{L}_{\text{a},k}\boldsymbol{C}_{\text{a}})\boldsymbol{w}_{\text{a},k} - \boldsymbol{L}_{\text{a},k}\boldsymbol{v}_{\text{a},k} \tag{3.14}$$

4

Kalman filter and the Heat Transfer Finite Element Model

4.1 Aluminum bar - Temperature observer simulation

The goal of the following simulations is to implement and analyze the performance of the Linear Kalman filter, both in the classic and in the augmented state form, estimating the temperatures along a synthetic aluminum bar. Moreover, we aim to use the less amount of temperature "sensors" (readout points) as possible.

In the simulation environment, the plant is the continuous time 1-D heat transfer finite element model, with N nodes and E finite elements. The state space representation of this system is:

$$\Upsilon_{\mathrm{B}} : \begin{cases} \dot{\boldsymbol{\theta}}(t) = \boldsymbol{\Phi}\boldsymbol{\theta}(t) + \boldsymbol{\Gamma}\boldsymbol{u} \\ \boldsymbol{T}(t) = \boldsymbol{\Psi}\boldsymbol{\theta}(t) \end{cases} \tag{4.1}$$

with

$$\boldsymbol{\Phi} = -(c\rho\boldsymbol{D}_{\mathrm{B}})^{-1}(\lambda\boldsymbol{H}_{\mathrm{B}} + \kappa\boldsymbol{K}_{\mathrm{B}}), \qquad \boldsymbol{\Gamma} = (c\rho\boldsymbol{D}_{\mathrm{B}})^{-1}\begin{bmatrix} \boldsymbol{q}_{\mathrm{in}} & \lambda\boldsymbol{q}_{\mathrm{conv}} \end{bmatrix},$$
$$\boldsymbol{\Psi} = \mathbb{I}_{N\times N}, \qquad \boldsymbol{u} = \begin{bmatrix} Q_{\mathrm{in}} & T_{\mathrm{amb}} \end{bmatrix}$$

where $\boldsymbol{\Phi} \in \Re^{N\times N}$ and $\boldsymbol{\Gamma} \in \Re^{N\times 2}$. The values of c, ρ and κ are those shown in Table 4.2. While λ=7.71 W/m^2-K (between aluminum and air), this is the value

reported by NewTwen experts after calibrating the motor model parameters.

Regarding the matrices $\boldsymbol{D}_{\mathrm{B}}$, $\boldsymbol{K}_{\mathrm{B}}$, $\boldsymbol{H}_{\mathrm{B}}$ and the vector $\boldsymbol{q}_{\mathrm{conv}}$, they are determined as shown in eq. 2.18, using the bar geometrical characteristics listed in Table 4.1.

The model input $\boldsymbol{u} \in \mathfrak{R}^2$ is a vector than comprises a manipulated and a non-manipulated component. The former is the amount of heat provided to the bar on its leftmost edge, Q_{in}, and the latter is T_{amb}, related to the heat exchanges with the ambient. Since Q_{in} acts exclusively in the first node of the FE mesh (x=0cm), $q_{\mathrm{in}} \in \mathfrak{R}^N$ in eq. 4.1 is a vector with zeros in all its entries but the first one. Then, when it is desired to add new manipulated heat sources acting in node j, it is only needed to create a vector of dimension N full of zeros with only the j-th entry equal to one, and concatenate it horizontally with the matrix $\begin{bmatrix} q_{\mathrm{in}} & \lambda q_{\mathrm{conv}} \end{bmatrix}$.

Length, L (m)	Height, h (m)	Width, w (m)
0.5	0.001	0.001

Table 4.1: Aluminum bar geometric characteristics

Density, ρ (kg/m^3)	Specific heat capacity, c (J/kg-K)	Thermal conductivity, κ (W/m-K)
2700	900	210

Table 4.2: Aluminum bar properties [11]

4.1.1 Model validation

Since the 1-D heat transfer model has been developed for an ideal body and there doesn't exist a physical bar, the calibration of this model is meaningless. However, we are using the experimental values of the aluminum properties, listed Table 4.2 and it is important to notice that the bar in much longer than thicker and then the 1-D heat transfer approximation is appropriate.

In what regards the model validation, in the absence of a real system to compare with, it is still important to consider the convergence and stability of the model solution. As it was mention is chapter 2, the finer the size of the finite elements, the more the approximated solution approaches the true one.

In principle, the smaller the elements, the better. Nevertheless, if the elements dimensions are too small, the solution might become unstable due to numeric dispersion.

To determine the appropriate spacial discretization step dx, we obtained the solution of the model Υ_B (eq. 4.1) for different dx using Simulink and setting Q_{in}= 500mW and T_{amb}= 25ºC. As can be seen in Figure 4.1, in steady state, as dx decreases the temperatures profile (mathematically) tends asymptotically to the actual true solution which is the limit when $dx \to 0$.

Now, having a look at the temperature time evolution at x= 10 cm, it can be seen in Figure 4.2 that in the first 20 s the curves corresponding to dx= 10 cm and dx= 5 cm goes below the ambient temperature (amplification in Figure 4.2b). This behavior is not proper of this phenomena, hence these dx's don't guarantee convergence of the solution to the actual one. It is observed, as before, that the smaller dx the temperature trajectories approach asymptotically the unique solution. If we would have decreased dx beyond 0.1 cm, the solution would not improve considerably. In view of this results, a good trade-off between solution convergence and simulation time is met when dx= 0.5 cm, which is the spacial discretization step used in all the simulations performed in this work.

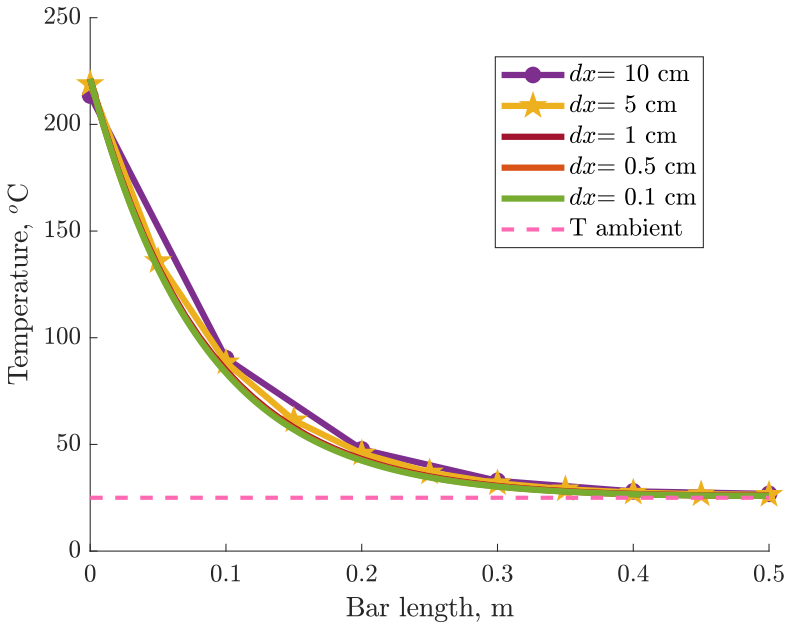

Figure 4.1: Ground truth temperatures for different dx at steady state (after 500 s). T_{amb} = 25ºC, Q_{in}= 500mW

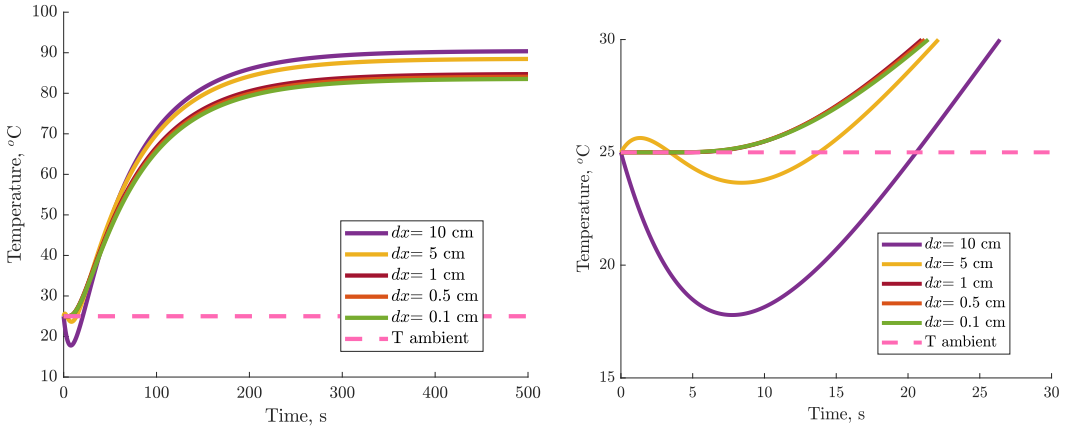

(a) (b)

Figure 4.2: Bar model temperature trajectories at $x = 10$ cm for different dx

4.1.2 Kalman filter implementation

As we explained in chapter 3, section 3.1.1, the success of the KF lies in the fidelity of the plant model and in its stabilizability and detectability. The bar model presented in eq. 4.1 is stabilizable. The system as it is, is completely observable, because the output $\boldsymbol{T}(t)$ is equal to the states vector $\boldsymbol{\theta}(t)$. However, we want to study the observability in the worse case, when there is only one temperature measurement available. That is, when the matrix $\boldsymbol{\Phi}$ is a row vector of N entries full of zero except for the entry that correspond to the node where the temperature wants to be known. After doing so the resulting system is still detectable. Hence, it has sense to apply the KF approach for our observer design having at least one temperature measurement.

Classic Linear Kalman Filter

The linear KF requires a discrete time linear model of the plant, access to the plant inputs and to at least one temperature measurement. The system model, Υ_{KF}, used to develop the linear KF was constructed from Υ_{B} modifying the matrix $\boldsymbol{\Phi}$ to get the temperatures readout only from the m nodes of interest and not of all nodes along the bar. Then, $\boldsymbol{\Phi} \in \Re^{m \times N}$. With the Υ_{KF} available, it was discretized using the *Exact* discretization method (see Table 2.1) with sampling time of 100ms, obtaining $\Upsilon_{\text{KF}}^{\text{dt}} = \{\boldsymbol{A}, \boldsymbol{B}, \boldsymbol{C}\}$

Finally, the Linear KF filter was implemented in Matlab & Simulink, it was programmed following the algorithm detailed in Algorithm 1.

Augmented state Linear Kalman Filter

In view of possible input uncertainties, or disruptions on a defined node of an external input with unknown magnitude, it was decided to implement an augmented estate Linear KF. To do so, the discrete time model $\Upsilon_{\text{KF}}^{\text{dt}}$ was modified adding as much states as inputs we consider to be uncertain, as explained in section 3.2. The augmented state discrete time system is in turn:

$$\Upsilon_{\text{aug}}^{\text{dt}}: \begin{cases} \begin{bmatrix} \boldsymbol{\theta}_{k+1} \\ \boldsymbol{d}_{k+1} \end{bmatrix} = \begin{bmatrix} \boldsymbol{A} & \boldsymbol{B}_d \\ \mathbf{0}_{n_d \times N} & \mathbb{I}_{n_d \times n_d} \end{bmatrix} \begin{bmatrix} \boldsymbol{\theta}_k \\ \boldsymbol{d}_k \end{bmatrix} + \begin{bmatrix} \boldsymbol{B} \\ \mathbf{0}_{n_d \times p} \end{bmatrix} \boldsymbol{u}_k \\ \boldsymbol{y}_k = \begin{bmatrix} \boldsymbol{C} & \mathbf{0}_{m \times n_d} \end{bmatrix} \begin{bmatrix} \boldsymbol{\theta}_k \\ \boldsymbol{d}_k \end{bmatrix} \end{cases}$$

notice that in this model, in comparison with the one in eq. 3.10, $\boldsymbol{C}_d = \mathbf{0}_{m \times n_d}$. This was done since any disturbance, from those considered in this work, acts directly on the output. The augmented KF was implemented in Matlab & Simulink, it was programmed following the algorithm detailed in Algorithm 1 using the model $\Upsilon_{\text{aug}}^{\text{dt}}$.

In Figure 4.3 it is shown the Simulink scheme developed and used for all the simulations concerning the aluminum bar temperature observer. Unless it is specified, the plant inputs are Q_{in}= 500mW and T_{amb}= 25^{o}C.

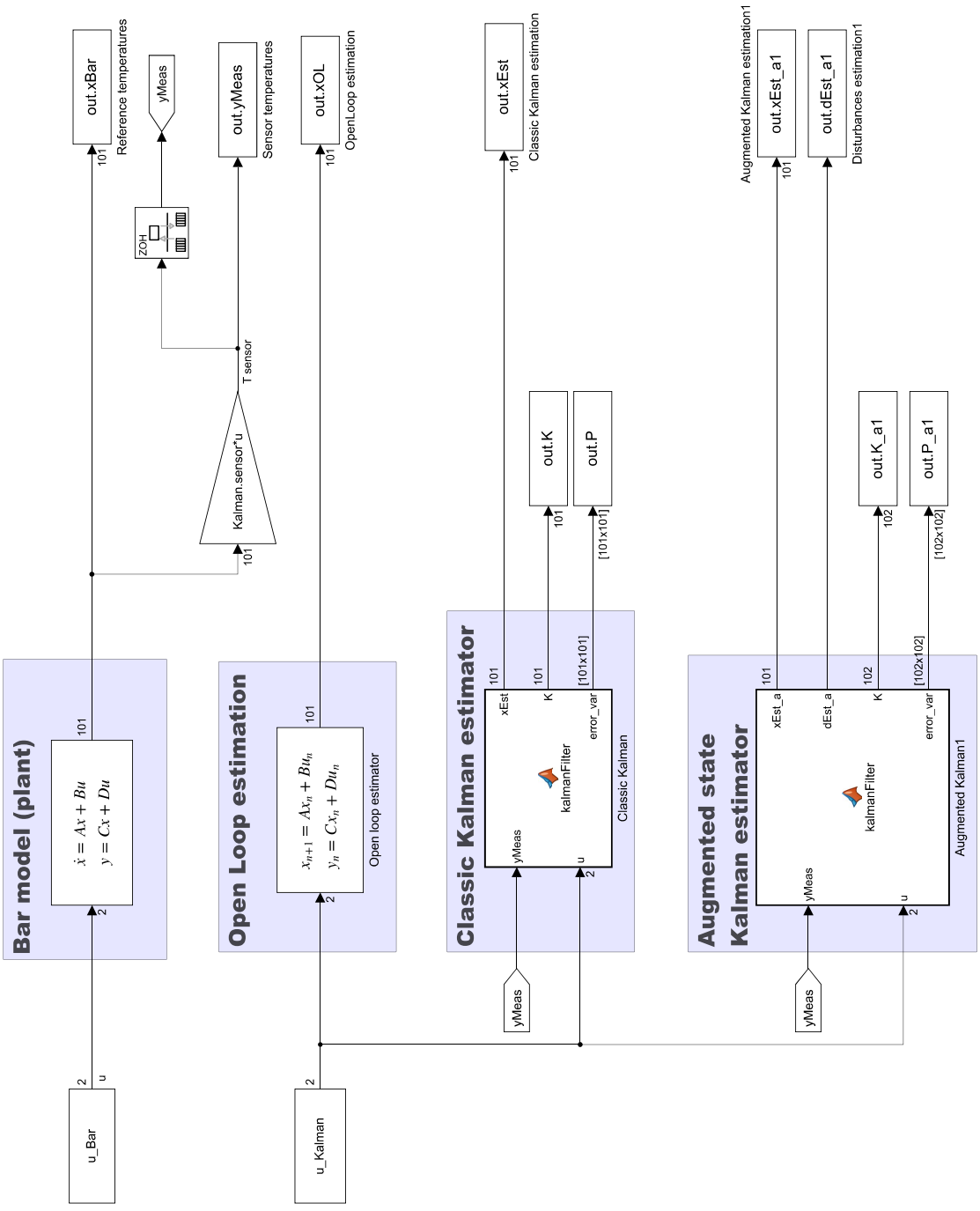

Figure 4.3: Simulink scheme developed for aluminum bar temperature observer

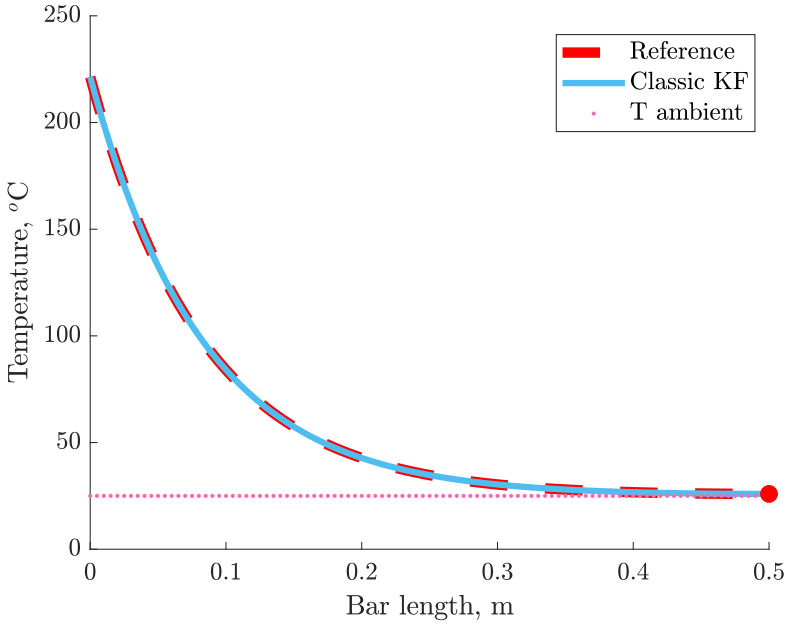

Figure 4.4: Classic KF implementation result. Actual and estimated temperatures along the bar at steady state. Red dot marks the temperature readout location

4.1.3 Classic Kalman Filter - Initial condition mismatch

In this section we will discuss the performance of the Linear Kalman filter to overcome initial condition mismatches. In this opportunity there is only one sensor available and it is positioned in the rightmost edge of the bar ($x = 50$ cm).

To show the capability of the Classic Linear KF to overcome initial conditions discrepancies, for the plant it was set $\boldsymbol{x}(t = 0) = T_{\text{amb}}$=25 °C. On the other hand, for the KF, $\hat{\boldsymbol{x}}(t = 0) = T_{\text{amb}} + 20$°C.

As it can be seen in Figure 4.4, lack of knowledge of the plant initial conditions doesn't prevent the KF from providing correct temperature estimation for all points along the bar at steady state. Although, as can be appreciated in Figure 4.5, where q are the entries of $\boldsymbol{Q}_w$ main diagonal, the time required for the estimation error to reach steady state increases as the uncertainty about the model increases, i.e. as q is bigger. Then, the higher the confidence in the model, the better the estimation of the temperature trajectories, obtaining not only good steady state results. This results were obtained considering zero measurement noise, therefore the diagonal entries (r) of $\boldsymbol{R}_v$ are all close to zero ($r = 1 \times 10^{-9}$)

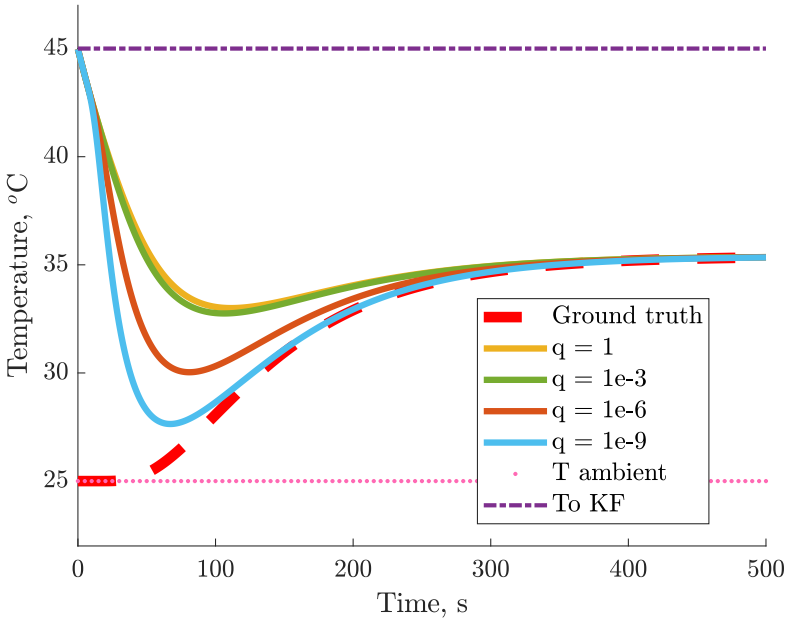

Figure 4.5: Classic KF implementation result. Temperature trajectories at x = 25cm for different $\boldsymbol{Q}_w$. Sensor placed at x = 50cm

4.1.4 Input uncertainties

Up to now the Kalman Filter has been feed with exactly the same plant inputs. This ideal situation is never met in reality, since KF inputs are quantities susceptible to uncertainties. For instance, while measuring the ambient temperature, it is possible that the temperature sensor readout are different from the one experience by the plant, because the sensor and the system might be far apart, the sensor could have some defect, or any other reason. It is also possible existence of another internal or external heat source not considered in the model formulation, like proximity of the plant to a functioning machine, sunbeams warming known parts of the plant, etc. These are uncontrollable inputs that may affect the system state and hence its state estimation. In order to built a KF robust against this kind inputs uncertainties, it was implemented the state augmentation explained in section 3.2.

In order to implement this approach, it is important to identify where the uncertainties come from and how they modify the system state to choose the right $\boldsymbol{B}_d$. To this end, it will be useful to write the input matrix $\boldsymbol{B}$ in a more convenient way. Each column of this matrix is associated with one input, then $\boldsymbol{B}$ could be written as $\boldsymbol{B} = \begin{bmatrix} \boldsymbol{b}_{\text{in}} & \boldsymbol{b}_{\text{conv}} \end{bmatrix}$, first column related to Q_{in} and the second one to T_{amb}.

Uncertainties in Q_{in}

We want to model disturbances acting on Q_{in}, then $\boldsymbol{B}_d = \boldsymbol{b}_{\text{in}}$ is the most appropriate choice.

As for the previous tests, the KF input was 500mW but the actual plant input is now equal 1 W, 100% different. In Figure 4.6 it is shown the actual and estimated temperatures along the bar at steady state. The temperatures estimations were determined from measurements done placing a sensor in position x= 25cm, the red bold dot in the graph. It is clear that the classic KF is not able to overcome this important input discrepancy, with estimation errors reaching almost 30 % before (see Figure 4.6a). The augmented state KF does a much better job with estimation errors practically imperceptible. This is not surprising since the classic KF doesn't have the information the augmented one has by means $\boldsymbol{B}_d$ about how the unknown input affects the state.

At the same time, the augmented KF is able to estimate correctly the amount of heat (ΔQ_{in}) provided to the bar that was missing in the KF input, as it is

evidenced in Figure 4.7. In this figure it is also shown that the time to reach steady state decreases as long as the confidence in the model increases, it is as the diagonal entries of Q_w decrease.

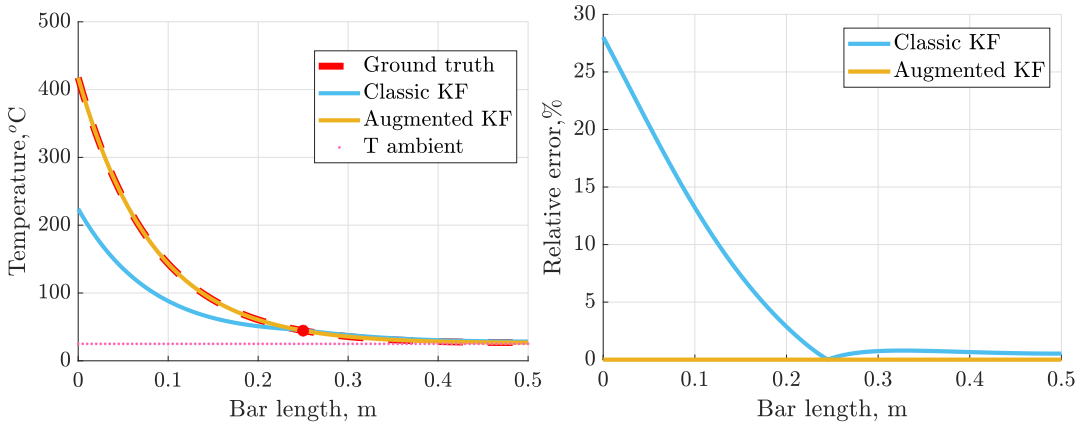

(a) Temperature estimation along the bar (b) Estimation error along the bar

Figure 4.6: KFs performance comparison at steady state for Q_{in} uncertain. **Plant input**: 1W, **KF input**: 0.5W. Temperature readout location marked as a red dot

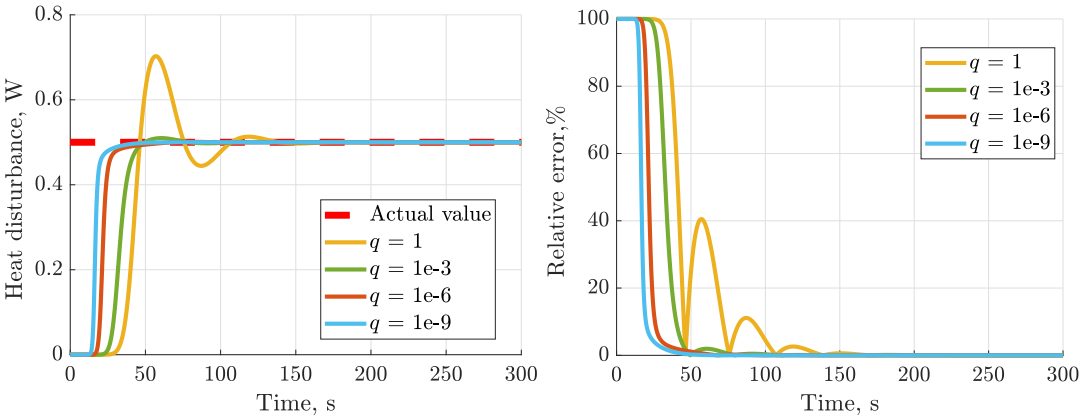

(a) Uncertainty estimation (b) Estimation error

Figure 4.7: Estimation of ΔQ_{in} for different Q_w. Temperature readout @ x= 25cm

It is important to notice that in addition to the variations on Q_w, the location of the sensors modifies the time required to reach zero estimation error. In Figure 4.8 it is presented the temperature trajectories at x= 0 cm for different Q_w when the only available sensor is placed in two different points, x= 50 cm and x= 25 cm. For a $Q_w = \mathbb{I}$ (worse scenario shown), a sensor located in the mid position of the bar allows us to reach steady state close to 100 s, while a sensor positioned in the rightmost edge of the bar increases that time to 300 s. If we look at

Figure 4.6a, the rightmost node that initially was at ambient temperatures as all the rest, doesn't modify its temperature considerably at steady state compared with its initial condition. Hence, the amount of information that a sensor located there carries will be less than a sensor positioned closer to the heat source.

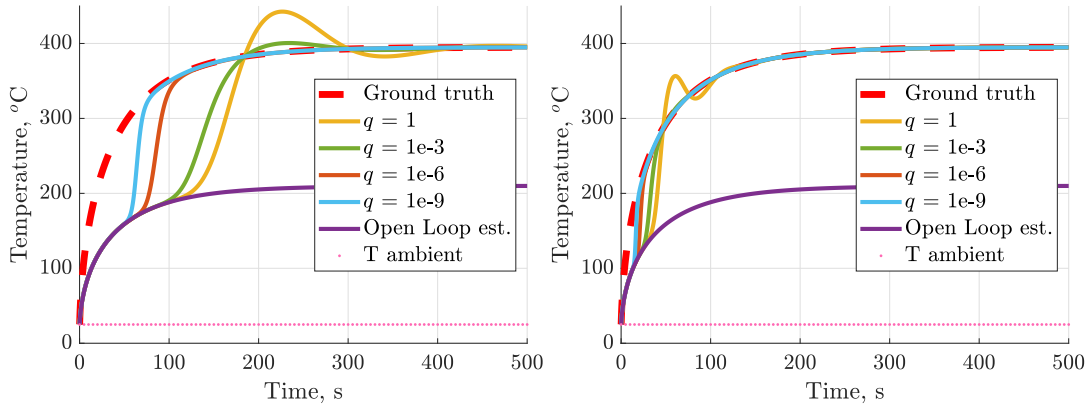

(a) Temperature readout at x = 50cm (b) Temperature readout at x = 25cm

Figure 4.8: Temperature trajectories at x = 5 mm for different $\boldsymbol{Q}_w$ and for two different location of temperature readout. **Plant** q_{in}= 1W, **KF** $\hat{\text{Q}}_{\text{in}}$= 500 mW

Uncertainties in T_{amb}

We would like to include possible uncertainties on T_{amb} then $\boldsymbol{B}_d = \boldsymbol{b}_{\text{conv}}$. As for the previous tests, in the following simulation results, the KF T_{amb} is 25°C but the actual plant T_{amb} is equal to 50 °C, one more time 100% different.

In Figure 4.9 is presented the temperature profile along the bar at steady state, once placed a sensor in position x= 25cm. It can be noticed that the classic KF is not able to overcome important discrepancies in the ambient temperatures, while the augmented KF estimation overlaps the plant output.

As happened before, the augmented KF is able to estimate correctly, with negligible estimation error, the value of the temperature difference ΔT_{amb} between the bar ambient temperature and the one provided to the KF, as it is depicted in Figure 4.10. In this figure it is also shown that the time to reach steady state decreases as long as the confidence in the model increases. A good feature that this figure is representing is the capability of the observer to provide estimation errors smaller than 10 % in less than 100 s, which is indeed a nice property considering that the dynamics of the temperature is not so fast.

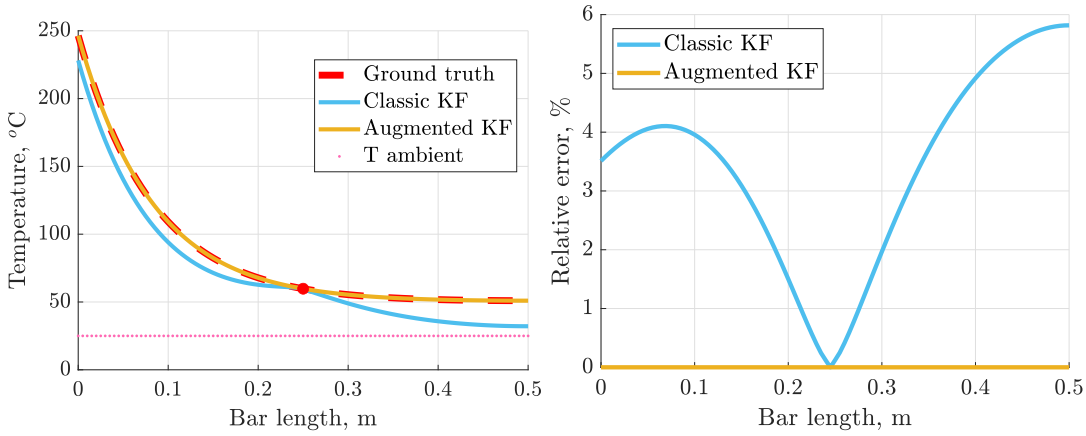

(a) Temperature estimation along the bar (b) Estimation error

Figure 4.9: KFs performance comparison at steady state for T_{amb} uncertain. **Plant** T_{amb}: 50°C, **KF** $\hat{T}_{amb}$: 25°C. Sensor @ x= 25cm, red dot

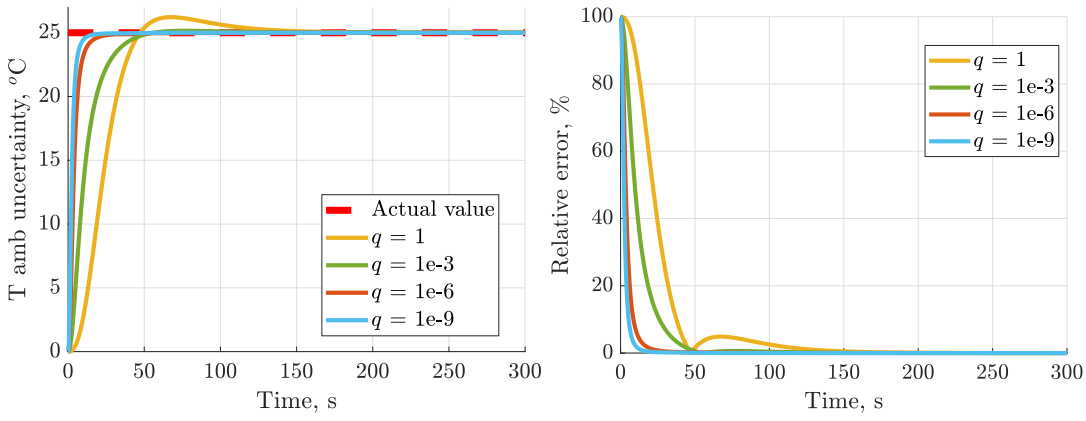

(a) Uncertainty estimation (b) Estimation error

Figure 4.10: Estimation of the disturbance state associated with T_{amb} for different Q_w. Temperature readout @ x= 25cm

Uncertainties in Q_{in} and T_{amb}

In order to prevent both Q_{in} and T_{amb} disruptions, $\boldsymbol{B}_d = \boldsymbol{B}$. In these simulations the plant inputs were Q_{in}= 1W and T_{amb}= 50^{o}C while the KF was feed with Q_{in}= 1W and T_{amb}= 50^{o}C.

We have seen before that with one input uncertain and one sensor, the augmented KF has been able to estimate perfectly the temperatures along the time (after 100 s) for all nodes along the bar. In this section we are including discrepancies between the plant and the KF for all two inputs. According to what was explained in section 3.2, it is needed at least as many sensors as disturbances to estimate correctly all the states (including the disturbances).

To study preliminary how the number of sensor and their locations modify the augmented KF performance, it was obtained the augmented state estimations using one sensor located each time at x = 12.5, 25, 37.5 and 50 cm. The results of these simulations are shown in Figure 4.11, where is it noticed that the smaller estimation error (> 5%) is obtained when the sensor is at x= 25cm. Consequently, it was possible to find good enough temperatures estimation even with only one sensor placed in a coordinate.

Later, adding a 2nd sensor, the situation improves unquestionably obtaining a practically zero estimation error at steady state. This last curve (in yellow) is showed overlapping the true values temperature in Figure 4.11a. The colored dots mark the sensor locations and the resulting estimation is drawn with the same dot color. Note that the sensor at x= 12.5cm was used to produce the estimation in orange and also the one in yellow, for that reason its edge is orange and its filling yellow.

If the requirement in the number of sensors is not met, the disturbance states (intrinsically non asymptotically stable) become unobservable and the estimation provided by the observer is not unique. As we saw, changing the sensor location the estimation changes.

The estimation of ΔQ_{in} and ΔT_{amb} with their respective estimation error are plotted in Figure 4.12. None of the estimations reached the actual value except for the one with two sensor and all the estimations were above 20 %.

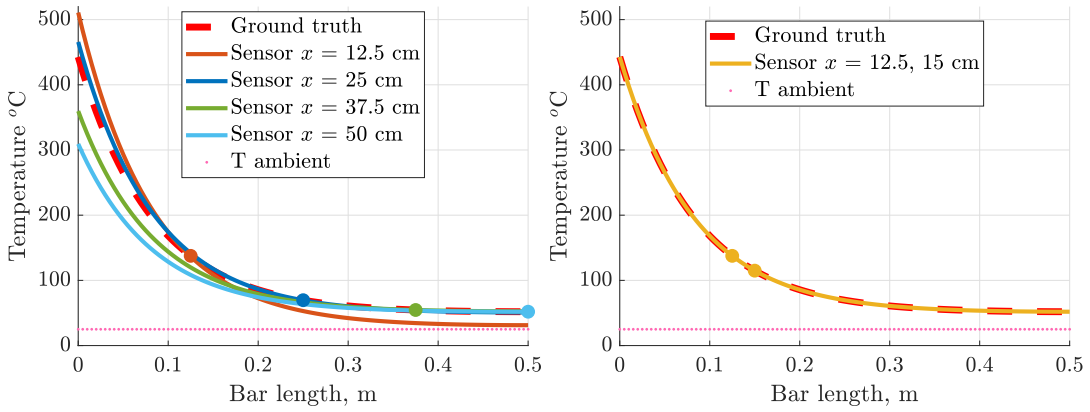

(a) Temperature along the bar (b) Temperature along the bar (2 sensors)

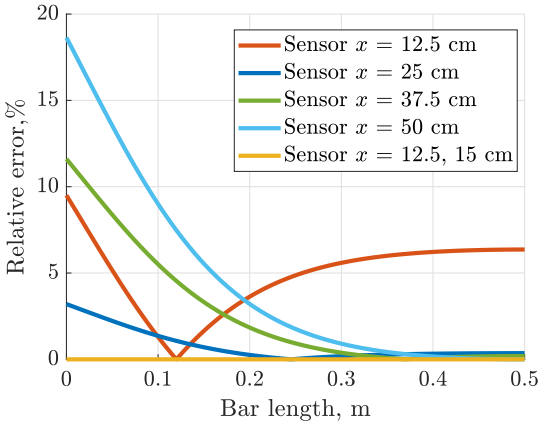

(c) Estimation error

Figure 4.11: KFs performance comparison at steady state for T_{amb} and Q_{in} uncertain with different temperature readout locations. **Plant inputs** T_{amb} = 50^{o}C, Q_{in} = 1W **KF inputs**: $\hat{T}_{amb}$: 25^{o}C, $\hat{Q}_{in}$ = 500mW.

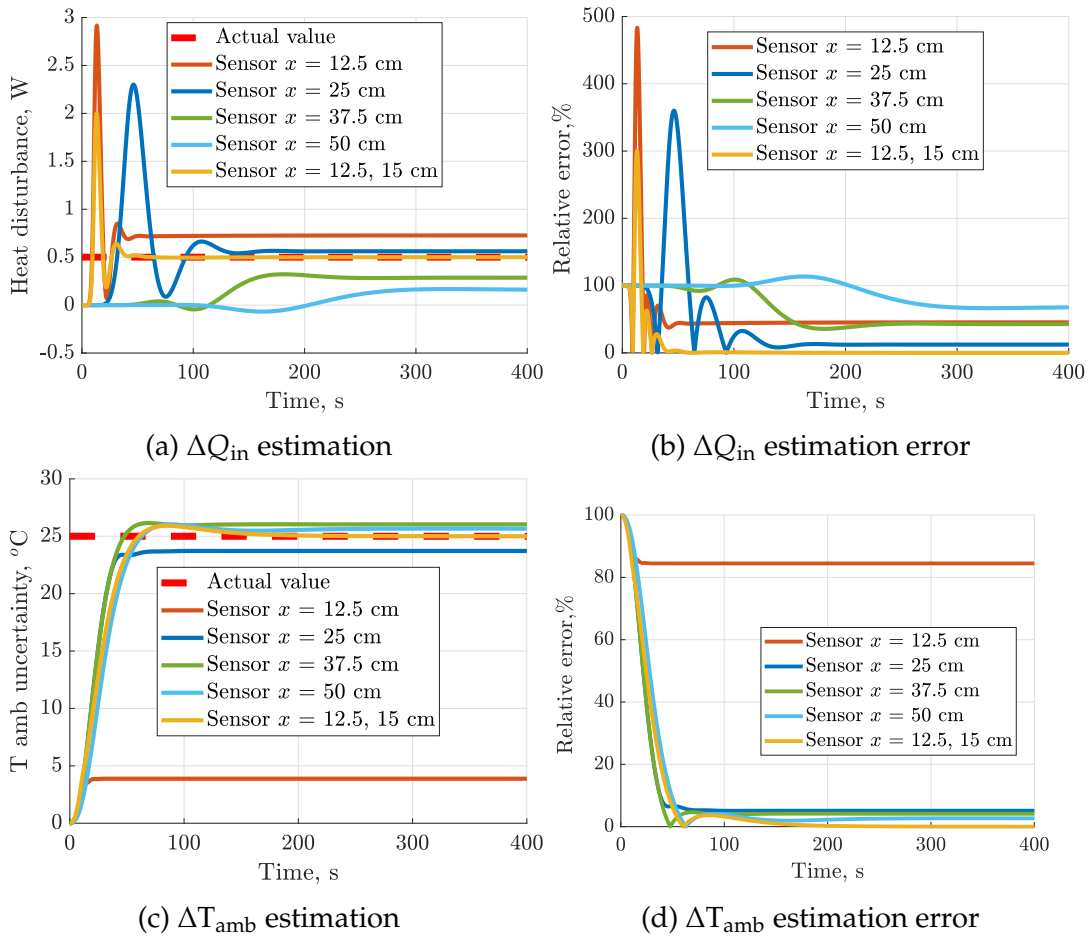

(a) ΔQ_{in} estimation

(b) ΔQ_{in} estimation error

(c) ΔT_{amb} estimation

(d) ΔT_{amb} estimation error

Figure 4.12: Estimation of disturbances associated with Q_{in} and T_{amb} for different temperature readout locations

Known and unknown external inputs

We have discuss up to this point the capability of the augmented state KF to overcome uncertainties in Q_{in} and T_{amb}. In this apart we will include both uncertainties sources in the state augmentation as well as a external heat source acting on a known node but of unknown magnitude.

For the following simulation results we consider for the KF: Q_{in}= 500mW and T_{amb}= 25°C; for the bar Q_{in}= 1W and T_{amb}= 50°C. It is considered that the bar experiences an external heat of 500mW at x=37.5cm (node 75). In the bar model the inclusion of a 3rd input is done adding a 3rd column ($\boldsymbol{b}_{\text{ext}}$) in the input matrix $\boldsymbol{B}$ as explained at the beginning of this chapter.

Once again, in this section we study the impact of the number of sensors in the quality of the estimation and as it can be appretiated in Figure 4.13, the more sensors the more accurate the estimation. Notice in Figure 4.13a that with one sensor the estimator doesn't not even notice the presence of the external input, it does a not that bad job estimating the temperatures close to the node where Q_{in} is present but the estimation error considerably increases as the distance to the sensor increases.

On the other hand, the inclusion of a 2nd sensor improves the observer performance being able to emulate the curve peak center ar x= 37.5cm an doing a really good estimation (>2 %) from x= 0 cm to x= 25cm where the estimation error is greater that 2 % but smaller than 10 %.

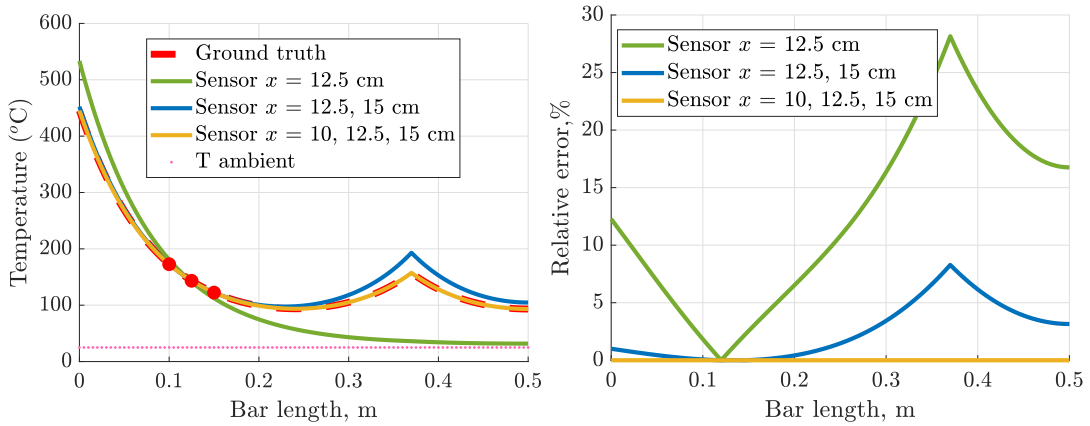

(a) Temperature estimation along the bar

(b) Estimation error

Figure 4.13: Augmented KF performance at steady state for T_{amb} and Q_{in} uncertain and an external heat source of unknown magnitude, with different number of temperature readouts. **Plant inputs** T_{amb} = 50°C, Q_{in} = 1W, Q_{ukn} = 500mW. **KF inputs**: $\hat{T}_{\text{amb}}$: 25°C, $\hat{Q}_{\text{in}}$ = 500mW.

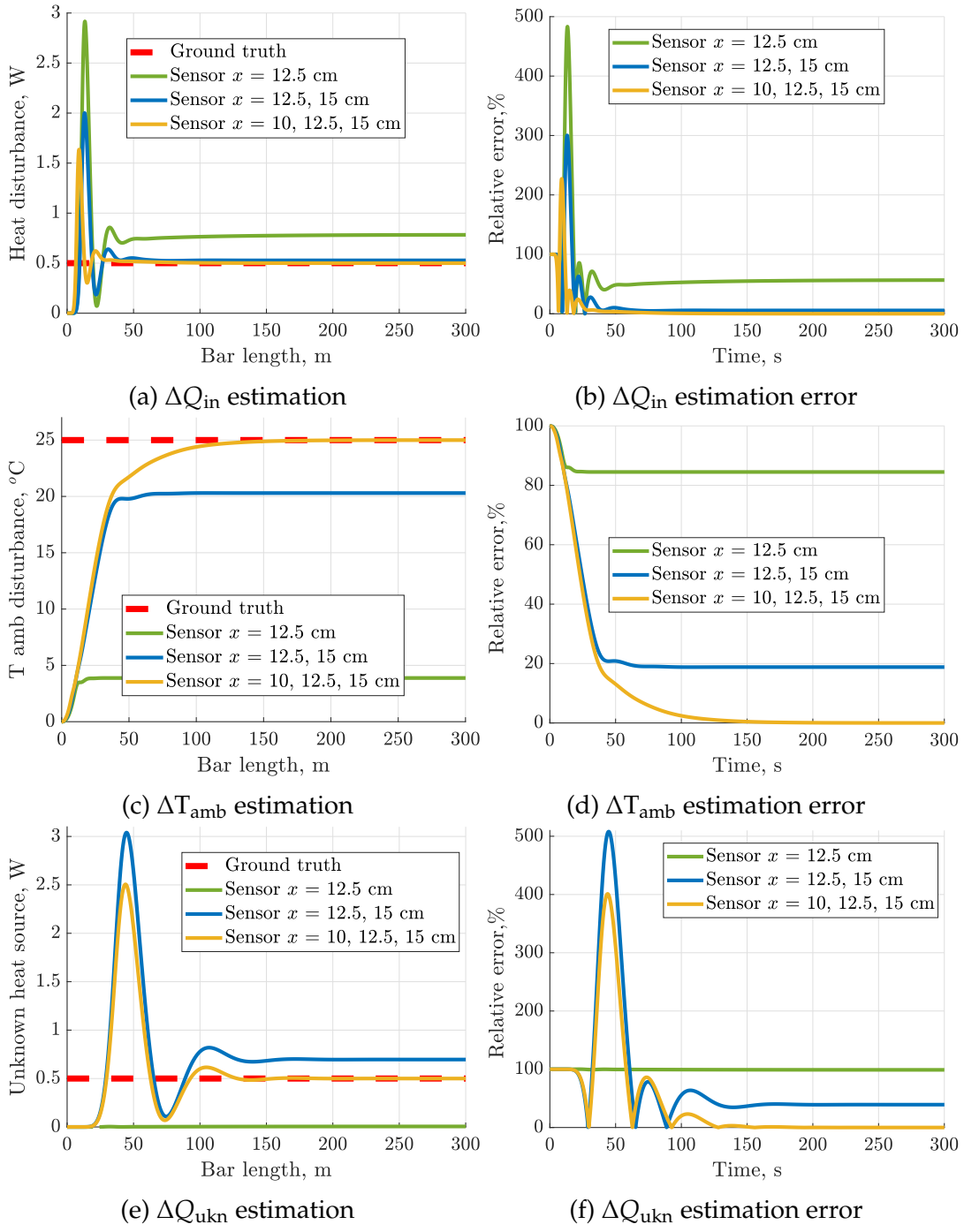

(a) ΔQ_{in} estimation

(b) ΔQ_{in} estimation error

(c) ΔT_{amb} estimation

(d) ΔT_{amb} estimation error

(e) ΔQ_{ukn} estimation

(f) ΔQ_{ukn} estimation error

Figure 4.14: Estimation of disturbance states associated with Q_{in}, T_{amb} and the unknown magnitude of external heat source for different number of temperature readouts

Apparently, the addition of a 3rd sensor solves all the problems and provides zero estimation error. This is not completely true. The last simulations are intended to show that the location of the sensors is very important. Maintaining

the input conditions, the three sensors originally located at x= 10, 12.5 and 15 cm were moved to x= 40, 42.5 and 45cm. The results are shown in Figure 4.15a. The second sensor set is not able to provide enough information about the head distribution along the bar, they reproduce perfectly the temperatures dynamics of all nodes after x= 37.5 cm but for nodes at $x < 37.5$ cm the estimation get worse since those sensors are not sensing the influence of the leftmost heat source.

On the other side, those sensors between the two heat sources are carrying enough information allowing the KF to estimate correctly the temperatures, ΔQ_{in}, ΔT_{amb} and Q_{ukn}, the magnitude of the heat source acting at x= 37.5 cm (Figure 4.16).

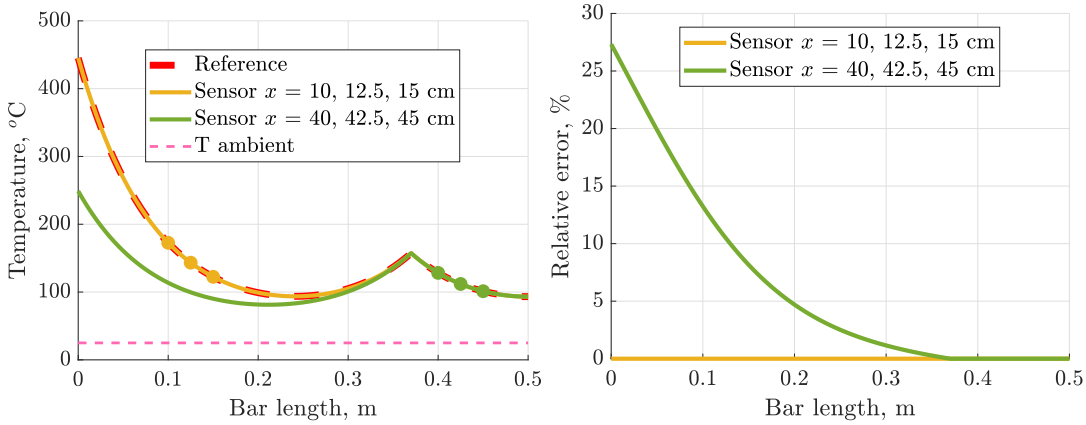

(a) Temperature estimation along the bar

(b) Estimation error

Figure 4.15: Augmented KF performance at steady state for T_{amb} and Q_{in} uncertain and an external heat source of unknown magnitude. Fixed number of temperature readouts but different locations. **Plant inputs** T_{amb} = 50°C, Q_{in} = 1W, Q_{ukn} = 500mW. **KF inputs**: $\hat{T}_{\text{amb}}$: 25°C, $\hat{Q}_{\text{in}}$ = 500mW.

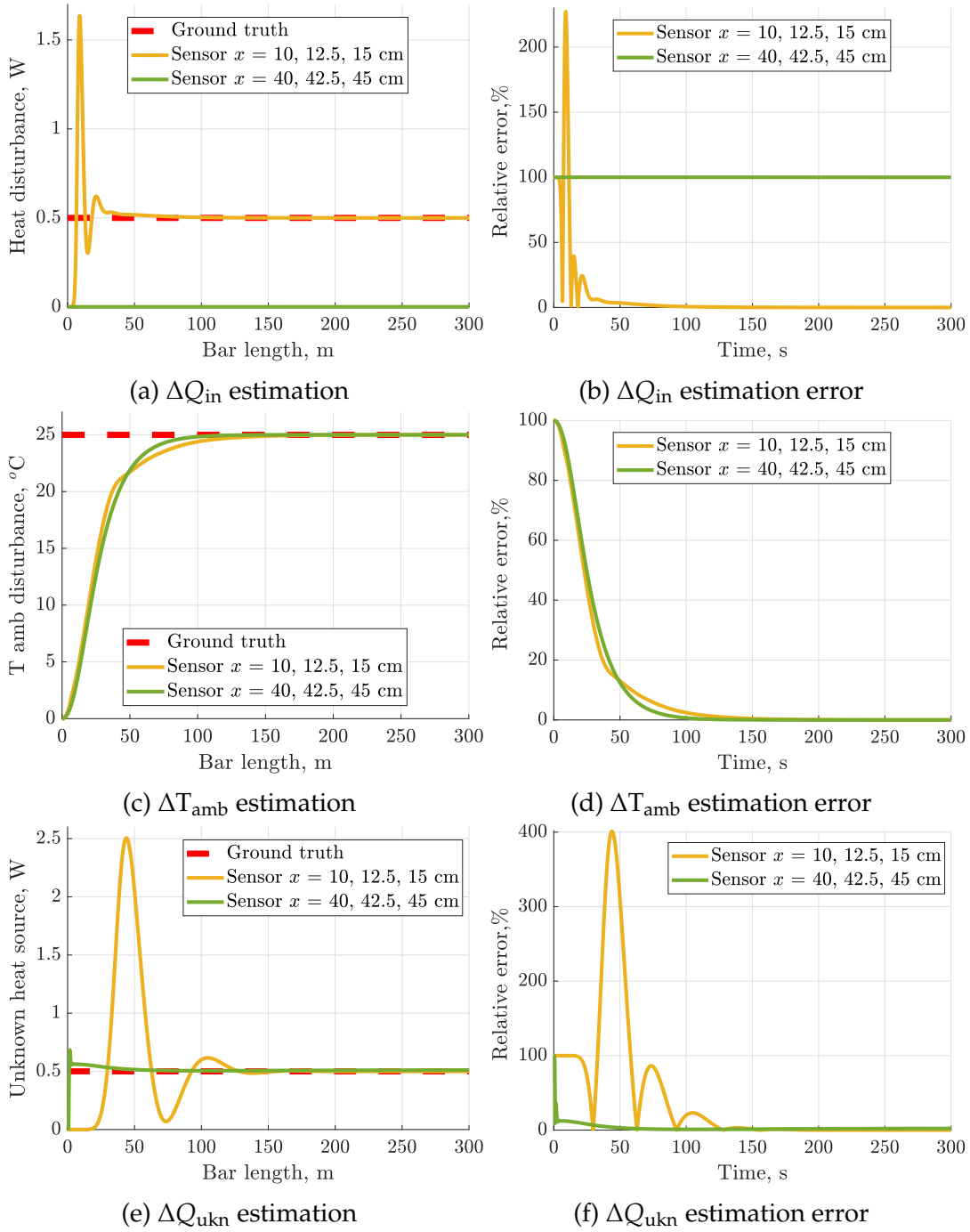

(a) ΔQ_{in} estimation

(b) ΔQ_{in} estimation error

(c) ΔT_{amb} estimation

(d) ΔT_{amb} estimation error

(e) ΔQ_{ukn} estimation

(f) ΔQ_{ukn} estimation error

Figure 4.16: Estimation of disturbance states associated with Q_{in}, T_{amb} and the unknown magnitude of external heat source for Fixed number of temperature readouts but different locations

4.2 PMS Motor - Temperature observer simulation

The goal of the following simulations is to implement and analyse the performance of the Linear Kalman filter, both classic and augmented state, estimating the temperature at eight points of interest of the PMS motor studied previously by the company NewTwen. As for the bar case, using the less amount of temperature sensors as possible.

In this simulations the plant is the reduced order continuous time 3-D heat transfer finite element model built for the motor in Figure 2.3. The model before reduction counts with N_f= 21046 nodes and a representation in state space as follows:

$$\Upsilon_{\mathrm{M}} = \begin{cases} \dot{\boldsymbol{\theta}}(t) = \boldsymbol{\Phi}\boldsymbol{\theta}(t) + \boldsymbol{\Gamma}\boldsymbol{u} \\ \boldsymbol{T}(t) = \boldsymbol{\Psi}\boldsymbol{\theta}(t) \end{cases} \tag{4.2}$$

with

$$\boldsymbol{\Phi} = -(\boldsymbol{D}_{\mathrm{M}})^{-1}(\boldsymbol{H}_{\mathrm{M}} + \boldsymbol{K}_{\mathrm{M}}), \qquad \boldsymbol{\Gamma} = (\boldsymbol{D}_{\mathrm{M}})^{-1}\begin{bmatrix} \boldsymbol{q}_{\mathrm{in}} & \lambda\boldsymbol{q}_{\mathrm{conv}} \end{bmatrix},$$
$$\boldsymbol{\Psi} = \mathbb{I}_{N\times N}, \qquad \boldsymbol{u} = \begin{bmatrix} \alpha I^2 & T_{\mathrm{amb}} \end{bmatrix}$$

where $\boldsymbol{\theta}(t) \in \Re^{N_f}$, the matrices $\boldsymbol{D}_{\mathrm{M}}$, $\boldsymbol{K}_{\mathrm{M}}$, $\boldsymbol{H}_{\mathrm{M}}$ and the vectors $\boldsymbol{q}_{\mathrm{in}}$, $\boldsymbol{q}_{\mathrm{conv}}$ are obtained as in eq. 2.15.

Due to the important amount of states, this system representation becomes non tractable as the temperatures are to be estimated node wise. In addition, the model calibration and validation would be an endless process. For that reason, as mentioned in section 2.4, the developers of the model used MOR techniques to obtain a state $\boldsymbol{x}(t) \in \Re^{N_{\mathrm{r}}}$ with $N_{\mathrm{r}} \ll N_f$ related with the full order one as $\boldsymbol{\theta}(t) = \boldsymbol{\Lambda}\boldsymbol{x}(t)$, where the columns of $\boldsymbol{\Lambda} \in \Re^{N_f \times N_{\mathrm{r}}}$ represent the basis for the reduced subspace [19].

After the MOR, the number of states was reduced to N_{r}= 17 and the representation of the reduced order model in state space is:

$$\Upsilon_{\mathrm{r}} : \begin{cases} \dot{\boldsymbol{x}}(t) = \boldsymbol{\Phi}_{\mathrm{r}}\boldsymbol{x}(t) + \boldsymbol{\Gamma}_{\mathrm{r}}\boldsymbol{u} \\ \boldsymbol{T}(t) = \boldsymbol{\Psi}_{\mathrm{r}}\boldsymbol{x}(t) \end{cases} \tag{4.3}$$

with

$$\mathbf{\Phi}_r = \mathbf{\Lambda}^T \mathbf{\Phi} \mathbf{\Lambda}, \qquad \mathbf{\Gamma}_r = \mathbf{\Lambda}^T \mathbf{\Gamma},$$
$$\mathbf{\Psi}_r = \mathbf{\Psi} \mathbf{\Lambda}, \qquad \boldsymbol{u} = \begin{bmatrix} \lambda I^2 & T_{amb} \end{bmatrix}$$

Comparing the systems Υ_M and Υ_r, both have as output the temperature of all the nodes in the FE mesh, $\boldsymbol{T}(t)$. Nonetheless, the states of Υ_M are the nodal temperatures itself while those of Υ_r don't have a clear physical meaning.

4.2.1 Model validation

Once obtained the reduced order model, which is the one used for the simulations developed in this work, it is required to calibrate and validate it in order to obtain the most appropriate parameters set that makes the model fit the real system behavior. The parameters are those related to the materials properties (c, λ, κ).

As far as the motor is concerned, the calibration and validation of its model was performed in advanced by the model developers. The resulting material parameters are presented in Table 4.3. The determined heat transfer coefficient, between aluminum (rotor) and air, is $\lambda = 7.71$ W/m^2-K.

Domain	Material	Density, ρ (kg/m^3)	Specific heat capacity, c (J/kg-K)	Thermal conductivity, κ (W/m-K)
Air gap	Air	1.204	1068	0.009
Rotor	Aluminum	2700	1349	121.4
Stator	Iron	7870	220	38.29
Winding	Copper	8940	470	173.6
PCB	Nylon	1150	1903	0.132

Table 4.3: Motor model parameters after calibration

4.2.2 Kalman filter implementation

We choose four points in the motor structure whose temperatures are used as ground truth to compare the KFs estimations with. The nodes are: 8624, (frontal flange), 100 (shaft), 3944 (rotor external surface) and 15520 (winding interior). At the same time, a fifth node (6587) was chosen to act as the place where a fictitious

thermocouple is, the location of this node coincides with the place where thermal sensors are usually placed in commercial motors. The temperature readout from the sensor node is the one used by the KFs to determine its estimates. Those points are highlighted in red in Figure 4.17.

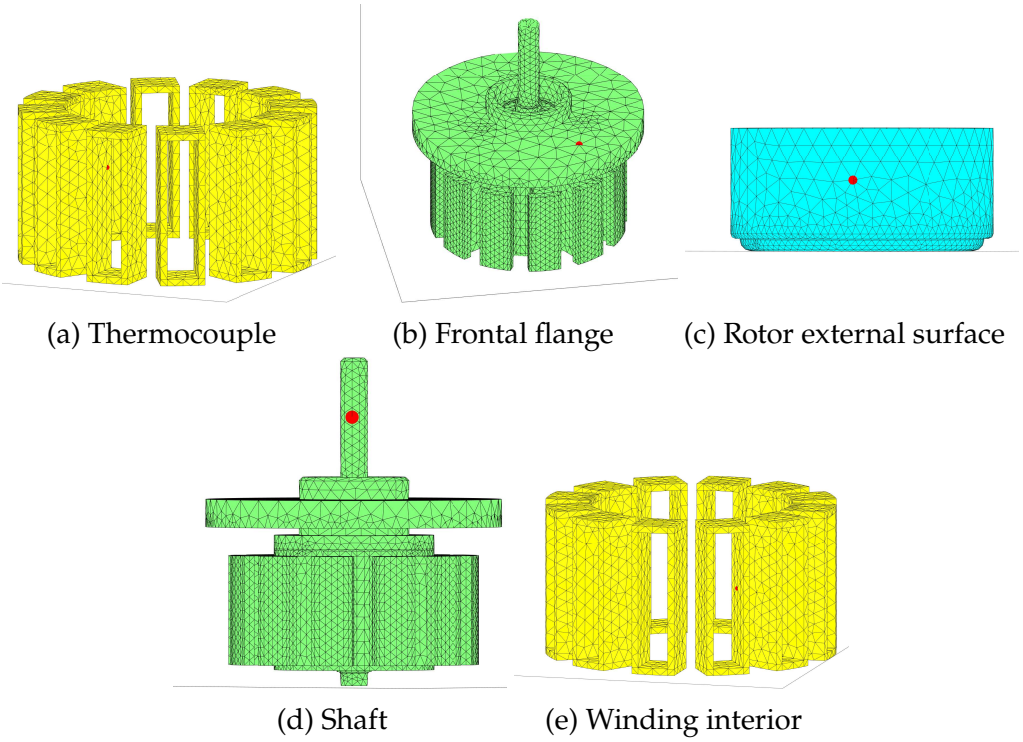

(a) Thermocouple (b) Frontal flange (c) Rotor external surface

(d) Shaft (e) Winding interior

Figure 4.17: Ground truth thermal points in the motor

To obtain as output, $\boldsymbol{y}(t)$, the temperatures at the nodes of interest and not at all nodes of the FE mesh, the matrix $\boldsymbol{\Psi}_\mathrm{r}$ in system Υ_r needs to be modified. The i-th row of $\boldsymbol{\Lambda}$ is responsible for the transformation of $\boldsymbol{x}(t)$ into the temperature at i-th node in the motor mesh. Then, to obtain the temperatures at the m nodes of interest, it is only needed to gather the corresponding m rows of $\boldsymbol{\Lambda}$ in a new matrix $\boldsymbol{V} \in \mathfrak{R}^{m \times N_\mathrm{r}}$ and multiply it by the state $\boldsymbol{x}(t)$, i.e. $\boldsymbol{y}(t) = \boldsymbol{V}\boldsymbol{x}(t)$. Hence the continuous time system used as physical system is:

$$\Upsilon_\mathrm{r} : \begin{cases} \dot{\boldsymbol{x}}(t) = \boldsymbol{\Phi}_\mathrm{r}\boldsymbol{x}(t) + \boldsymbol{\Gamma}_\mathrm{r}\boldsymbol{u} \\ \boldsymbol{y}(t) = \boldsymbol{V}\boldsymbol{x}(t) \end{cases} \tag{4.4}$$

with

$$\boldsymbol{\Phi}_\mathrm{r} = \boldsymbol{\Lambda}^\mathrm{T}\boldsymbol{\Phi}\boldsymbol{\Lambda} \qquad \boldsymbol{\Gamma}_\mathrm{r} = \boldsymbol{\Lambda}^\mathrm{T}\boldsymbol{\Gamma} \qquad \boldsymbol{u} = \begin{bmatrix} \lambda I^2 & T_\mathrm{amb} \end{bmatrix}$$

Classic Linear Kalman Filter

The linear KF requires a discrete time linear model of the plant, access to the plant inputs and to temperature measurements. Consequently, the system Υ_r (of eq. 4.4) was discretized using the *Exact* discretization method (see Table 2.1) with sampling time of 100ms, obtaining $\Upsilon_r^{dt} = \{\boldsymbol{A}, \boldsymbol{B}, \boldsymbol{C}\}$.

The success of the KF lies in the fidelity of the plant model and in its stabilizability and detectability. All the modes of the system are such that their modulus are inside the unit circle, hence in case of non observability and/or controllability, the non observable and/or non controllable subsystems are asymptotically stable. So, no matter the number of sensors or their locations, the system is detectable and stabilizable.

In the following simulations we will use primarily the thermocouple node as temperature measurement point but, when it is required the addition of a second sensor, the node in the frontal flange will be used as well. The sensor choice is done gathering in $\boldsymbol{V}$ the rows of $\boldsymbol{\Lambda}$ that correspond to the node we want to measure on.

Figure 4.18 shows the singular values (in logarithmic scale) of the observability matrix of Υ_r^{dt} obtained using each of the just mentioned sensors separately and both of them together. It is appreciated that with one sensor, regardless its position, the singular values are practically the same and most of them considerably smaller than 1. In fact, there is only one greater than one. With two sensors, the singular values increase some orders of magnitude, but this increment is not significant since there are only two > 1, all the rest are still much smaller than one. In principle, the sensor location should be reconsidered to reach higher observability degree. Nevertheless, we will emulate the case in which the sensor location is given by the manufacturer, as is the case of the thermocouple, and we will add a second sensor in an accessible position.

Finally, the linear KF filter was implemented in Matlab & Simulink and programmed following the algorithm detailed in Algorithm 1.

Augmented state linear Kalman Filter

To account for possible input uncertainties, it was decided to implement an augmented state linear KF. To do so, the discrete time model Υ_r^{dt} was modified adding as much states as inputs we consider to be uncertain, as explained in section 3.2. The augmented state discrete time system is in turn:

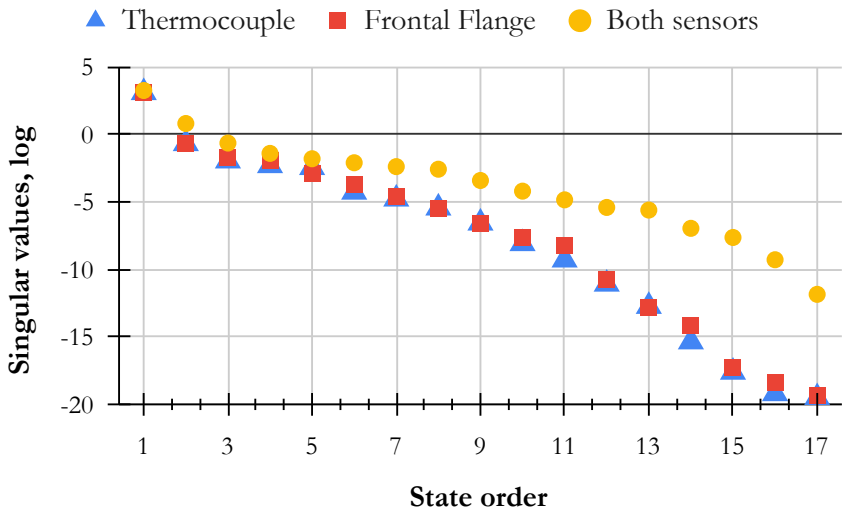

Figure 4.18: Singular values of $\Upsilon_{\mathrm{r}}^{\mathrm{dt}}$ observability matrix for different sensors choice

$$\Upsilon_{\mathrm{aug}}^{\mathrm{dt}}: \begin{cases} \begin{bmatrix} \boldsymbol{x}_{k+1} \\ \boldsymbol{d}_{k+1} \end{bmatrix} = \begin{bmatrix} \boldsymbol{A} & \boldsymbol{B}_d \\ \mathbf{0}_{n_d \times N_{\mathrm{r}}} & \mathbb{I}_{n_d \times n_d} \end{bmatrix} \begin{bmatrix} \boldsymbol{x}_k \\ \boldsymbol{d}_k \end{bmatrix} + \begin{bmatrix} \boldsymbol{B} \\ \mathbf{0}_{n_d \times p} \end{bmatrix} \boldsymbol{u}_k \\ \boldsymbol{y}_k = \begin{bmatrix} \boldsymbol{V} & \mathbf{0}_{m \times n_d} \end{bmatrix} \begin{bmatrix} \boldsymbol{x}_k \\ \boldsymbol{d}_k \end{bmatrix} \end{cases}$$

with n_d being the number of disturbances. Notice that in this model, in comparison with the one in eq. 3.10, $\boldsymbol{C}_d = \mathbf{0}_{m \times n_d}$. This was done since any disturbance, from those considered in this work, acts directly on the output.

According to [15], the observability (detectability) of the augmented state system is granted if the following conditions hold true: **1)** $\Upsilon_{\mathrm{r}}^{\mathrm{dt}}$ is observable (detectable), **2)** the number of sensors is at least the number of disturbances and **3)**

$$\operatorname{rank}(\boldsymbol{M}) = \operatorname{rank} \begin{bmatrix} (\mathbb{I} - \boldsymbol{A}) & -\boldsymbol{B}_d \\ \boldsymbol{C} & \mathbf{0}_{n_d \times n_d} \end{bmatrix} = N_{\mathrm{r}} + n_d \tag{4.5}$$

Regarding **1)**, the detectability of $\Upsilon_{\mathrm{r}}^{\mathrm{dt}}$ is granted. In what respect the number of sensors, we will consider at most two input disturbances so, with two sensors available **2)** holds. About **3)**, the lank of rank of that matrix is prevented if $\Upsilon_{\mathrm{r}}^{\mathrm{dt}}$ is detectable and the columns of $\begin{bmatrix} \boldsymbol{B}_d & \mathbf{0}_{n_d \times n_d} \end{bmatrix}^{\mathrm{T}}$ are linearly independent. The latter, is always true for the two kind of disturbances studied in this work, since

we start from the premise that the disturbances sources are completely known.

The augmented state linear KF filter was implemented in Matlab & Simulink and programmed following the algorithm detailed in Algorithm 1 using the system Υ_{aug}^{dt}.

In Figure 4.3 it is shown the Simulink scheme developed and used for all the simulations concerning the motor temperature observer. Unless it is specified, the motor inputs are $I(t)$= 1 A and T_{amb}= 24.75 ^{o}C.

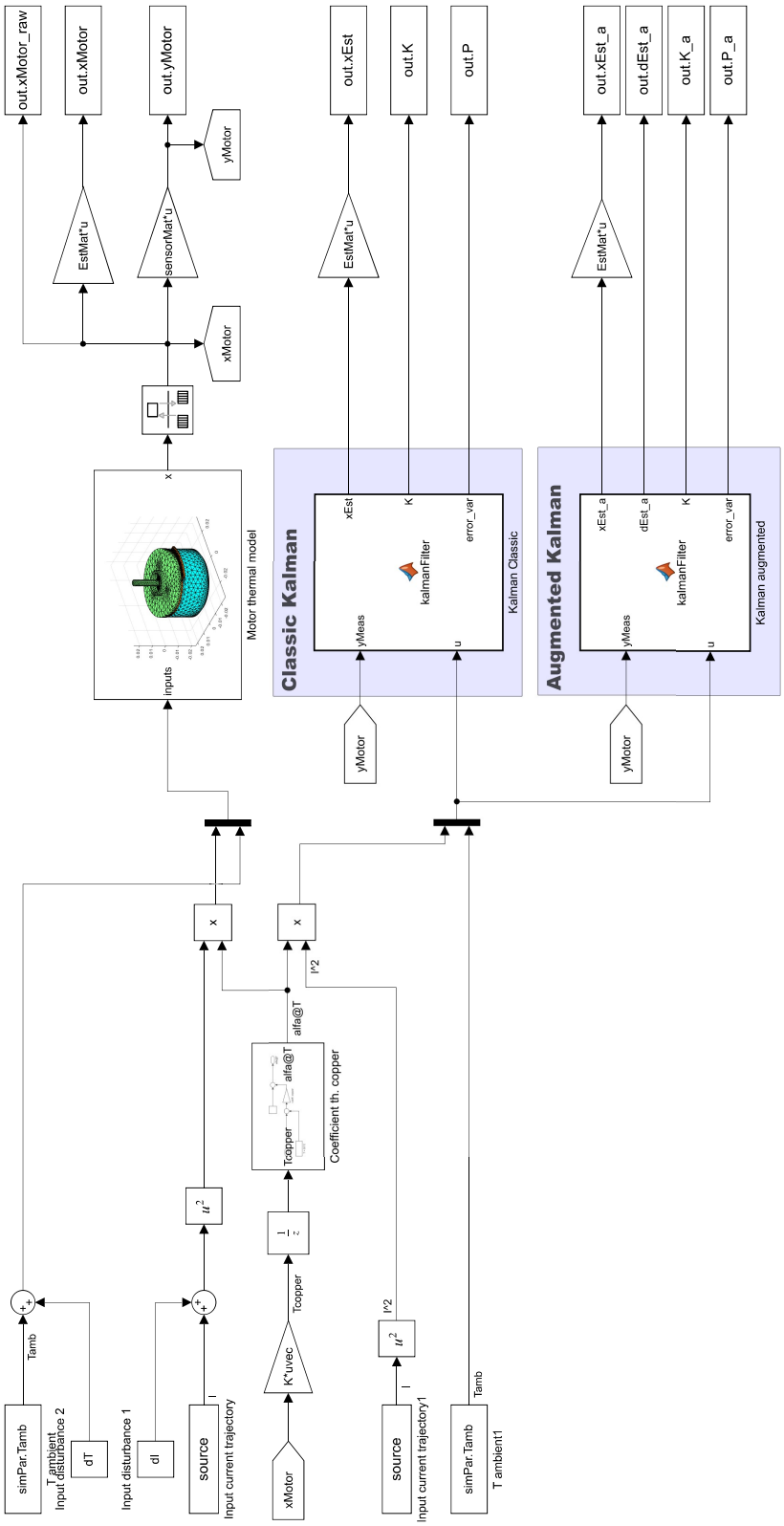

Figure 4.19: Simulink scheme developed for PMS motor temperature observer

4.2.3 Input uncertainties

As it was consider in the case of the bar, section 4.1.4, we will study the capability of the classic and augmented state KFs overcoming input uncertainties when the motor, a system more complex than the bar, is concern.

In this opportunity, we will let the plant and the KF inputs to be different. First, we consider two separate cases, differences in the current ($I(t)$) and then discrepancies in the ambient temperature (T_{amb}). Lastly, variations in both the current and the ambient temperature are examined.

To implement the augmented state KF, it is important to identify where the uncertainties come from and how they modify the system state to choose the right $\boldsymbol{B}_d$. As it was done for the bar, $\boldsymbol{B}$ can be written as $\boldsymbol{B} = \begin{bmatrix} \boldsymbol{b}_{\text{in}} & \boldsymbol{b}_{\text{conv}} \end{bmatrix}$, where the first column is related to $I(t)$ and the second one to T_{amb}.

Uncertainties in $I(t)$

To overcome disturbances acting on $I(t)$, $\boldsymbol{B}_d = \boldsymbol{b}_{\text{in}}$ is the right choice. The difference between the motor current and the one provided to the KFs is 0.1 A (10 % of difference). In principle, with one sensor the detectability of the augmented system is obtained and the augmented state KF should be able to prevail over this discrepancy. However, when running the simulations considering only the thermocouple readout, there is no difference between the classic and augmented state KFs. For that reason it was decided to include the other available sensor, the one in the frontal flange, and re-run the simulations. As it can be seen in Figure 4.21, for both KFs, 10% discrepancy in the input current does not impact considerably the temperature estimations, at least in the nodes whose temperatures are taken as ground truth. Along the time, the estimation error does not represent more than 0.1 % of the measurements.

Taking into consideration the estimation of the $N_{\text{r}} = 17$ states of the reduced order system, the augmented state KF reaches an important improvement compare with the classic KF estimation, as can be appreciated in Figure 4.22 and 4.23. In most of the cases, the classic KF commits an error of 100 %, there are some estimates with even higher errors, while the augmented state KF makes considerably smaller errors.

It is important to point out that there is one state, x_1, whose estimation is done accurately by both classic and augmented state KFs. This well done esti-

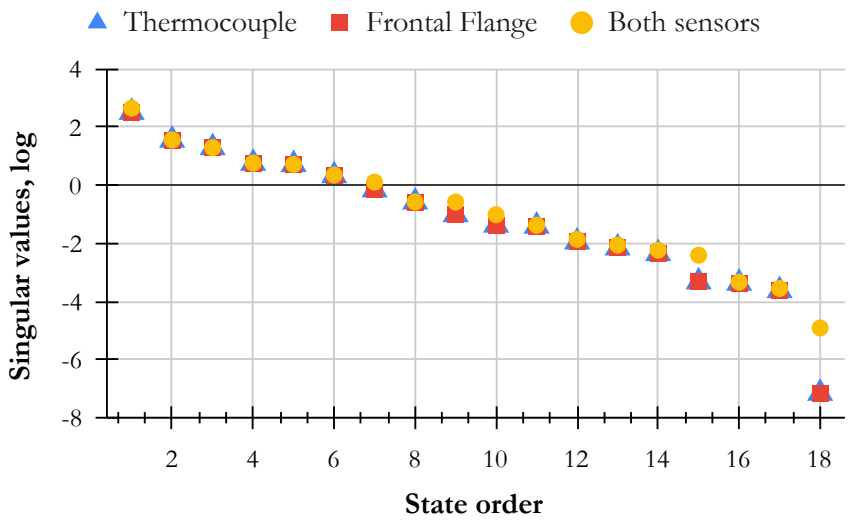

Figure 4.20: Singular values of matrix $\boldsymbol{M}$ (eq. 4.5)for different sensors choices

mation is the one allowing the classic KF to estimate correctly the temperatures at the interest points, because the weight associated with x_1 (in the linear transformation from the reduced space to the full order one) is at least 3 orders of magnitude higher than all the others.

It is still an open question why with a sensor it was not possible to observe differences between the classic and the augmented state KFs responses. The answer is related to the observability of the augmented state system. With only one sensor, the matrix $\boldsymbol{M}$ (eq. 4.5) losses its rank, while the conjunction of two sensors recovers the rank of $\boldsymbol{M}$. Referring to Figure 4.20, where the singular values of $\boldsymbol{M}$ are presented in logarithmic scale, it can be seen that regardless the number of sensors or their location, the singular values are all the same but the smaller one, whose value increases in five orders or magnitude when the second sensor is included.

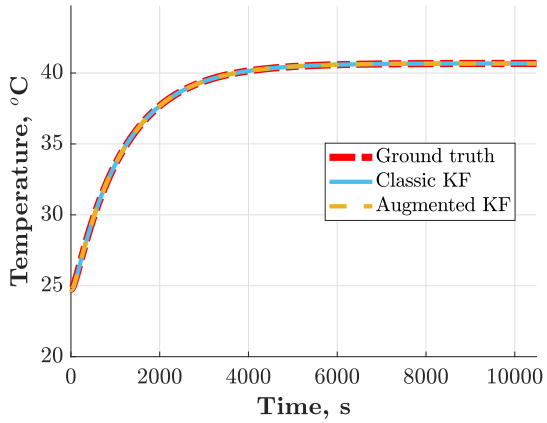

(a) Rotor external surface

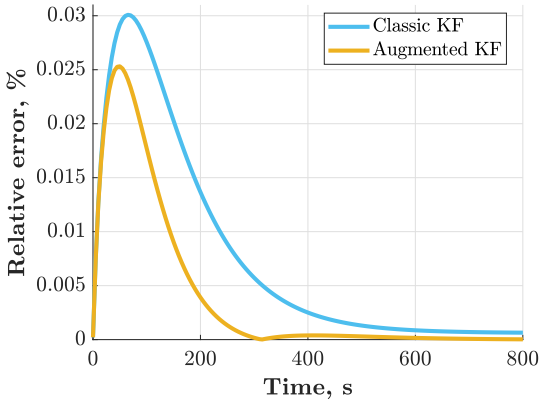

(b) Rotor ext. surface - Rel. error

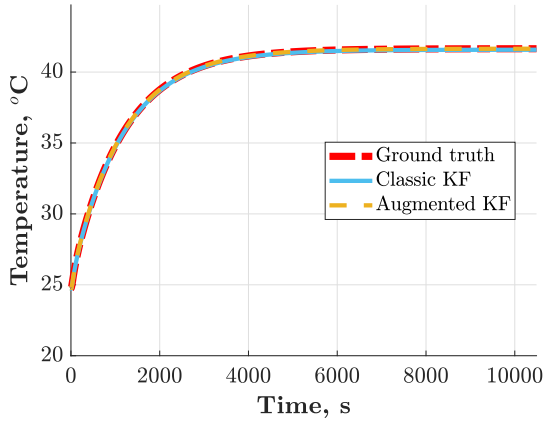

(c) Shaft

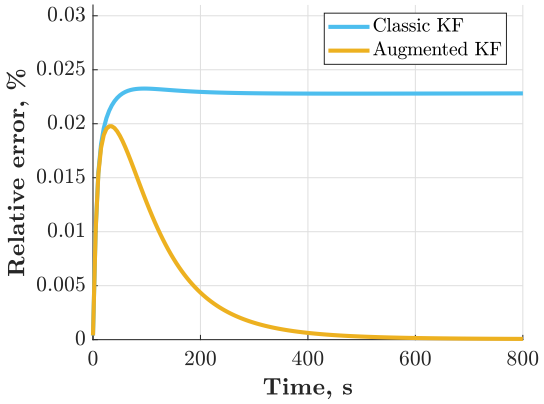

(d) Shaft - Rel. error

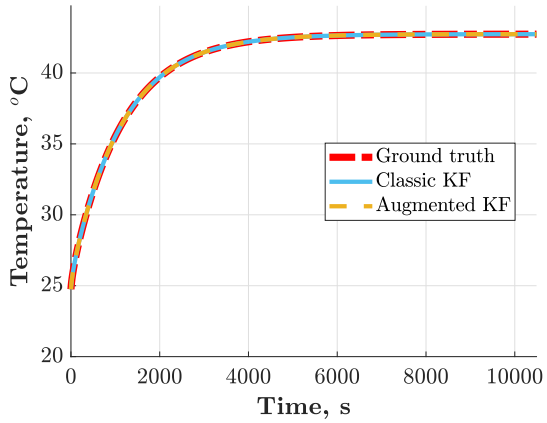

(e) Winding interior

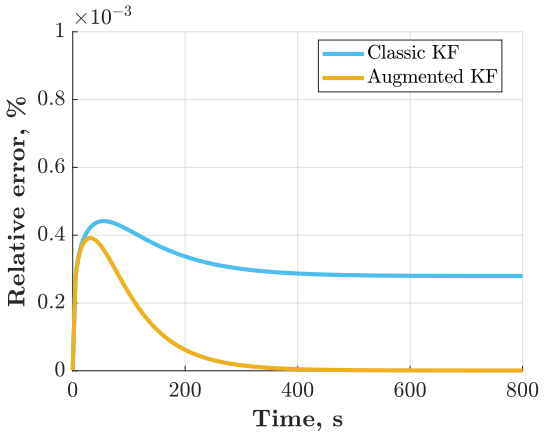

(f) Winding interior - Rel. error

Figure 4.21: Temperatures estimation. KFs performance comparison for $I(t)$ uncertain, $\boldsymbol{Q}_w = \mathbb{I}$. **Plant** $I(t)$: 1 A, **KF** $\hat{I}(t)$: 1.1 A.

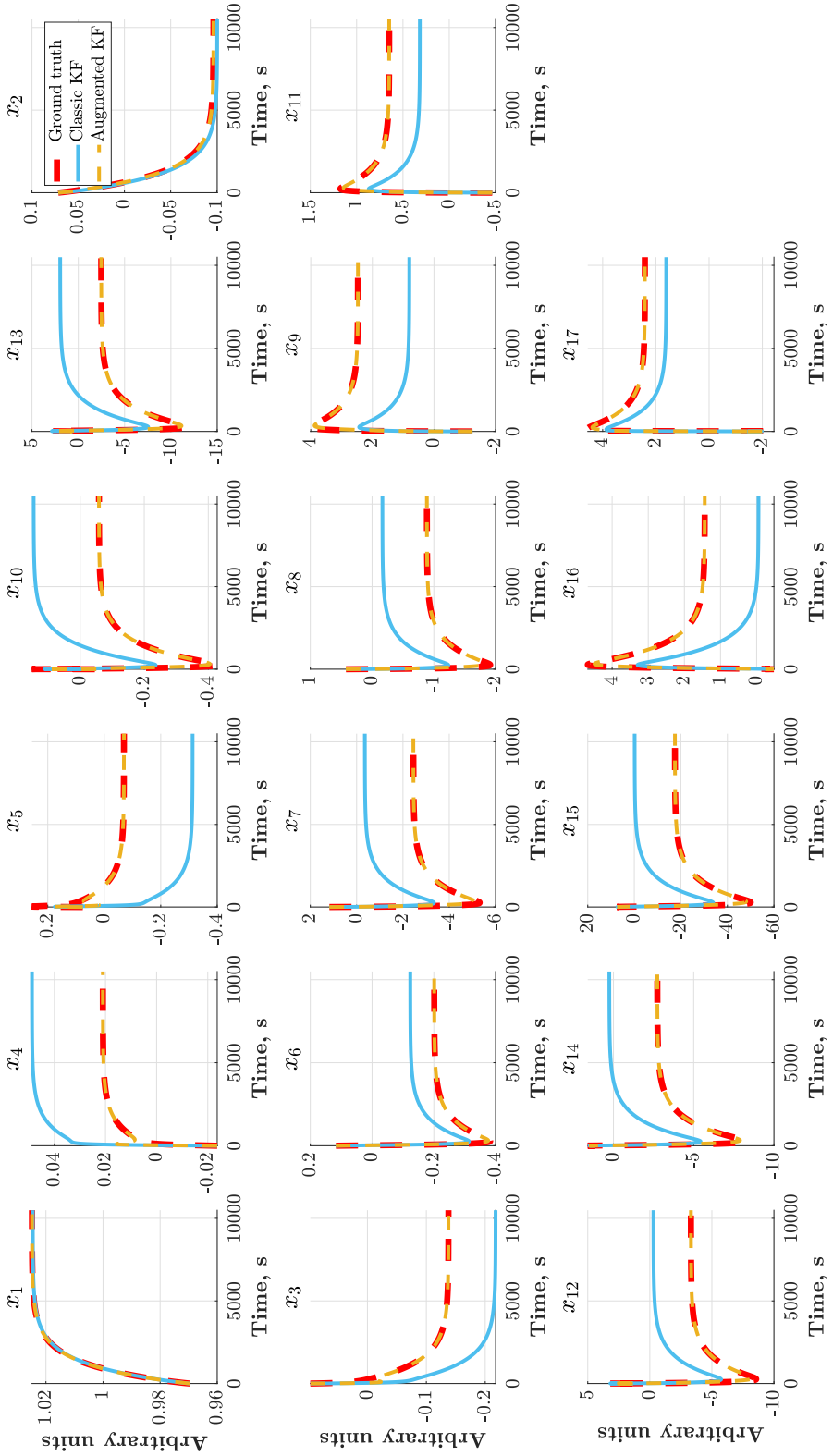

Figure 4.22: $\boldsymbol{x}(t)$ estimation. KFs performance comparison for $I(t)$ uncertain, $\boldsymbol{Q}_w = \mathbb{I}$. **Plant** $I(t)$: 1 A, **KF** $\hat{I}(t)$: 1.1 A.

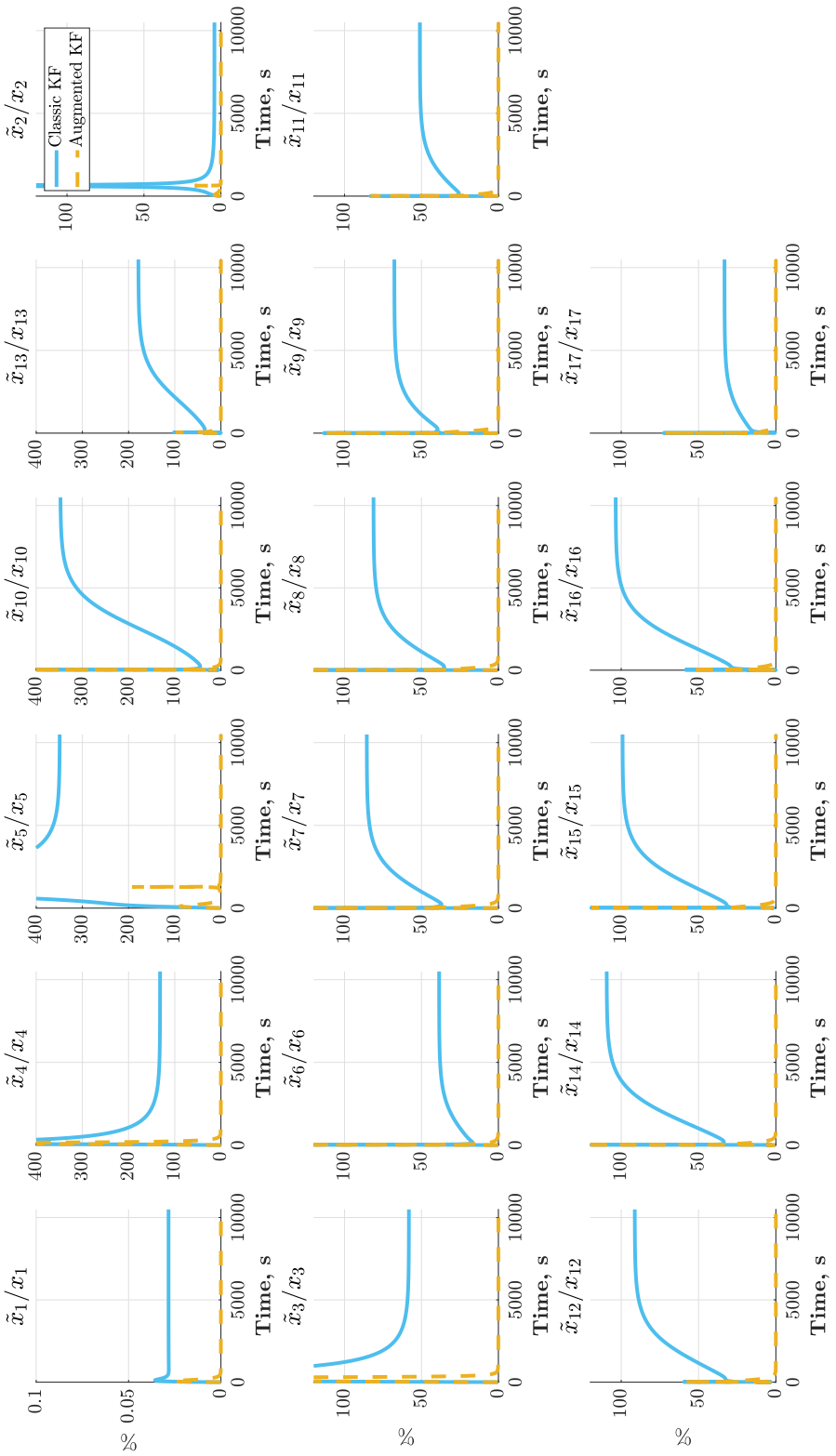

Figure 4.23: $\boldsymbol{x}(t)$ estimation error. KFs performance comparison for $I(t)$ uncertain, $\boldsymbol{Q}_w = \mathbb{I}$. **Plant** $I(t)$: 1 A, **KF** $\hat{I}(t)$: 1.1 A.

Uncertainties in Tamb

To overcome disturbances acting on T_{amb}, $\boldsymbol{B}_d = \boldsymbol{b}_{\text{conv}}$. The difference between the motor ambient temperature and the one provided to the KFs is 5 °C (20 % of difference). As it happened when analyzing uncertainties in $I(t)$, with only one sensor there is no difference between both KFs estimations and this behavior is associated with the lack of rank of the matrix $\boldsymbol{M}$. Then, two sensors were used to estimate the temperatures in the winding, shaft and external surface of the rotor.

In Figure 4.24, it can be noticed that both KFs estimations are good enough with an estimation error not greater than 0.2 % in the nodes considered as ground truth. However, the estimations of the augmented state KF have smaller errors compare with the classic KF response. At the same time, it worth to notice that the most affected part of the motor by changes in the ambient temperature is the rotor external surface, since it is in direct contact to the air, and in fact, is in this node where the classic KF makes the bigger errors.

Analyzing the estimates of $\boldsymbol{x}(t)$, shown in Figures 4.25 and 4.25, the classic KF makes errors at steady state between 0.1 % and 400 %. Nevertheless, this does not prevent him from making errors of less than 0.5 % estimating temperatures. The reason is the same explained in the previous case, when $I(t)$ was uncertain, both KF estimate well x_1, the state that matters most in the transformation between the reduced order space and the temperatures space.

Uncertainties in $I(t)$ and T_{amb}

In order to provide a complete analysis of the approach, it was intended to study the case where the two uncertainties act simultaneously on both inputs. However, with the two sensors considered up to now the matrix $\boldsymbol{M}$ was rank deficient. By adding a third sensor, the external node of the rotor, the matrix $\boldsymbol{M}$ still did not recover its rank. To study this case, a detailed analysis on where to place the sensors must be made.

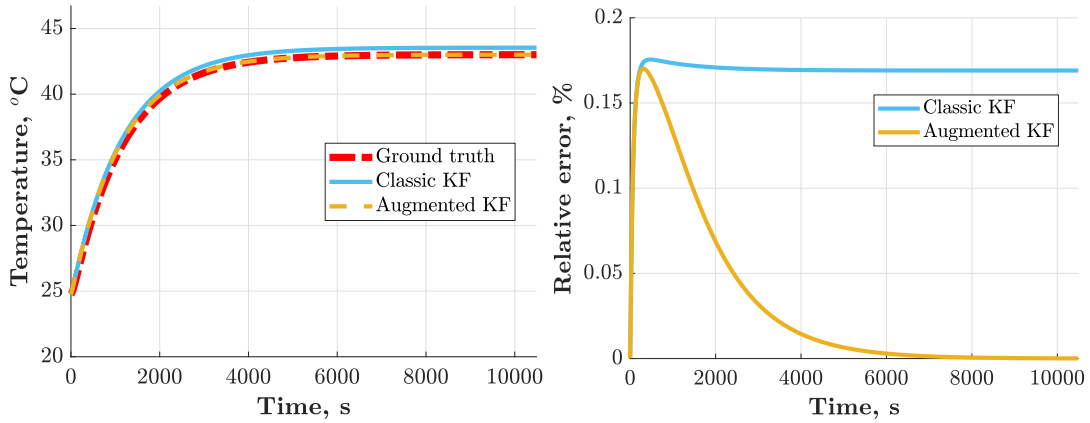

(a) Rotor external surface

(b) Rotor ext. surface - Rel. error

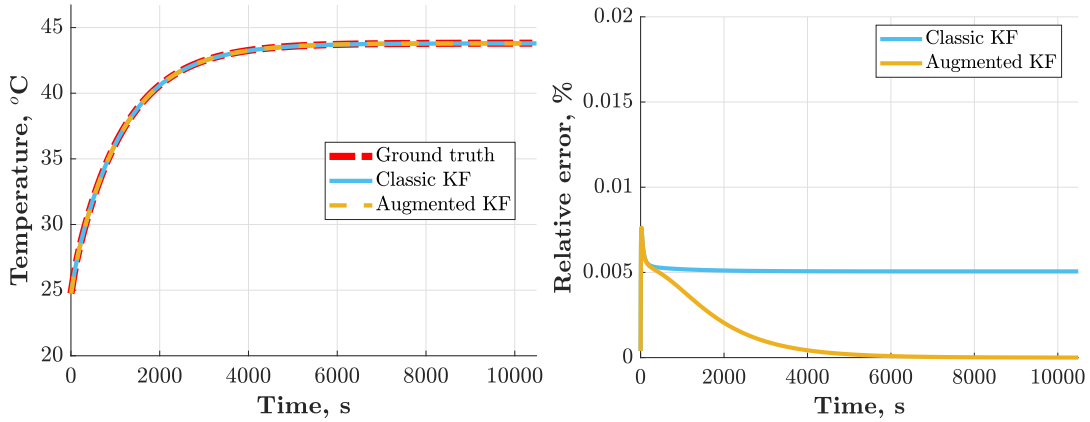

(c) Shaft

(d) Shaft - Rel. error

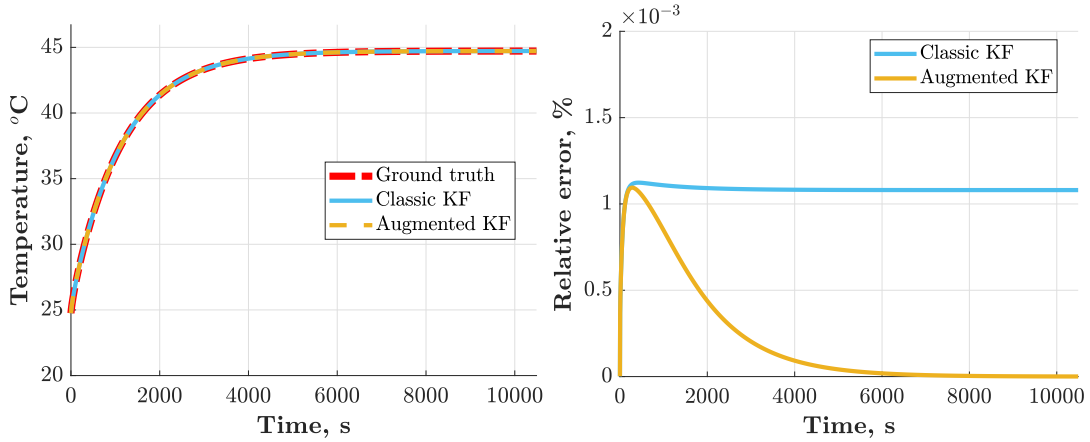

(e) Winding interior

(f) Winding interior - Rel. error

Figure 4.24: Temperatures estimation. KFs performance comparison at steady state for T_{amb} uncertain, $Q_w = \mathbb{I}$. **Plant** T_{amb}: 29.7°C, **KF** $\hat{T}_{amb}$: 24.7°C.

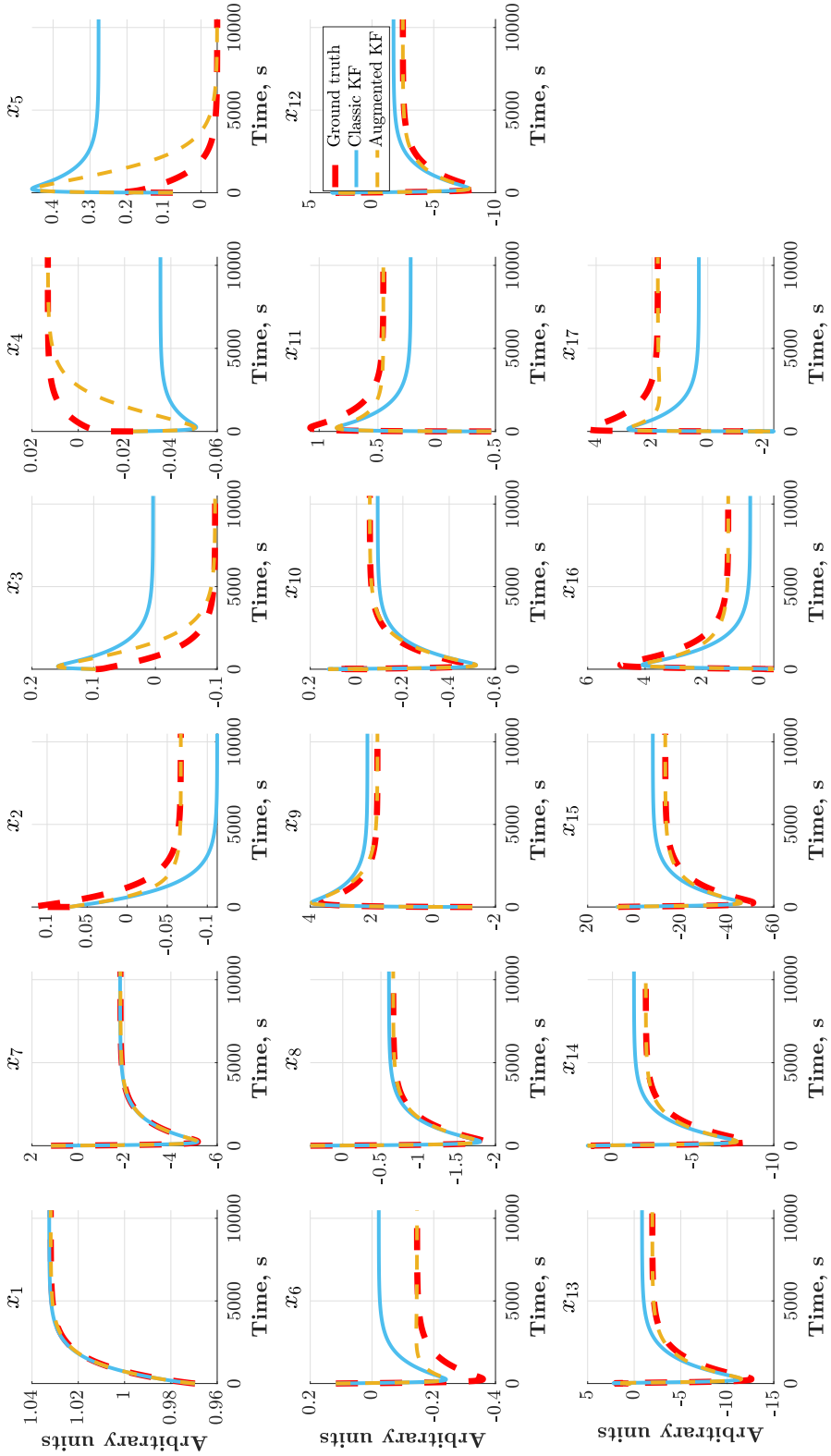

Figure 4.25: $\boldsymbol{x}(t)$ estimation. KFs performance comparison at steady state for T_{amb} uncertain, $\boldsymbol{Q}_w = \mathbb{I}$. **Plant** T_{amb}: 29.7ºC, **KF** $\hat{T}_{amb}$: 24.7ºC.

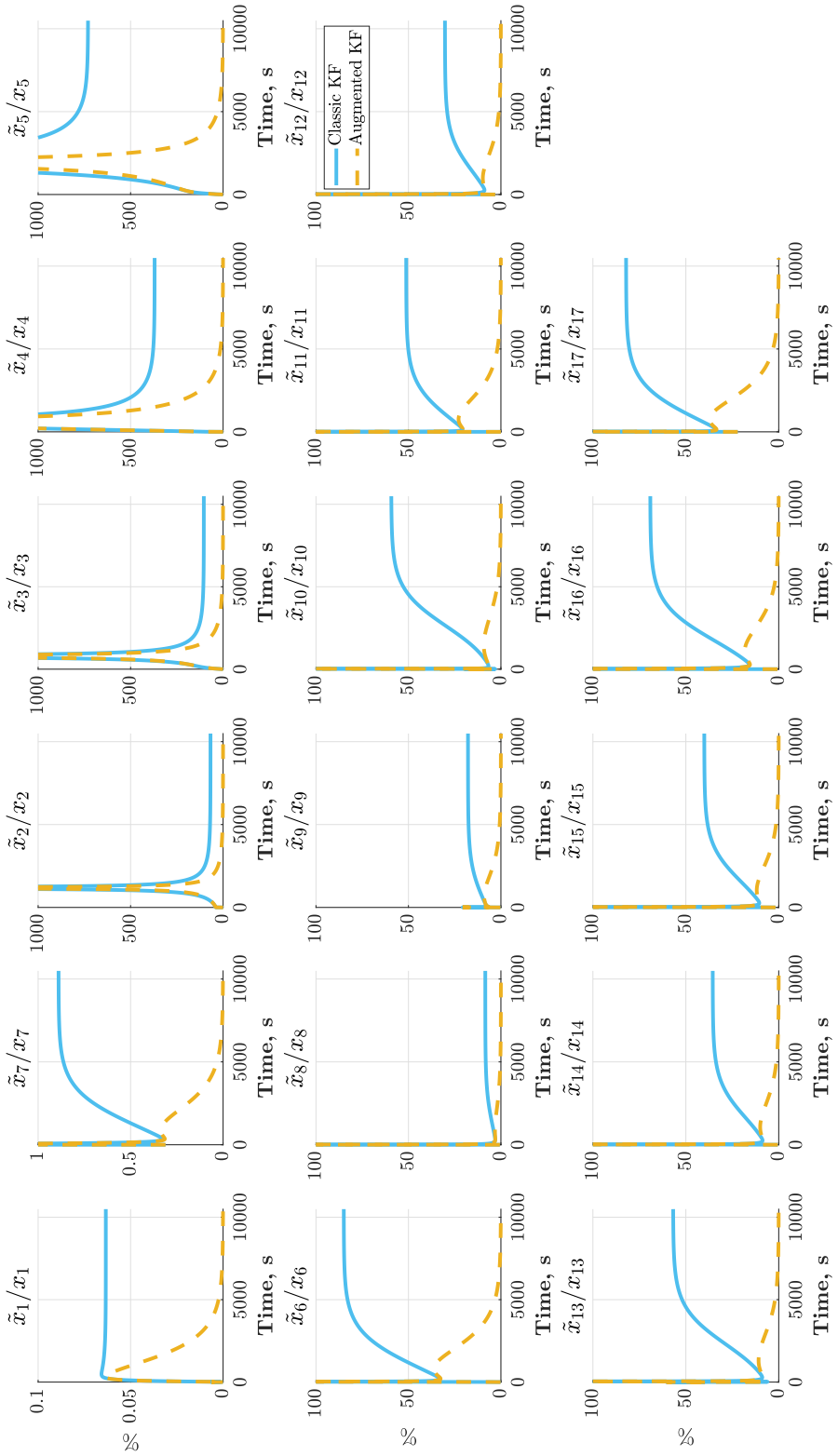

Figure 4.26: $x(t)$ estimation error. KFs performance comparison at steady state for T_{amb} uncertain, $Q_w = \mathbb{I}$. **Plant** T_{amb}: 29.7°C, **KF** $\hat{T}_{amb}$: 24.7°C.

5

Conclusions and Future Works

Having developed a detectable and stabilizable model of the solid bar and the Permanent Magnet Synchronous Motor, the systems whose temperatures want to be estimated, and knowing perfectly the plant inputs, the Linear Kalman filter (KF) algorithm constitute a good solution as thermal observer with only one sensor available, even if the initial conditions of the physical system are unknown. Reaching almost negligible estimation errors at steady state. With a right choice of the process noise covariance matrix and an appropriate location of the temperature sensor, it is possible to obtain an accurate estimate of the temperature trajectories even during part of the transient period, before the steady state condition is reached.

Additional requirements to the observer were posed, it needed to provide good estimates even with non perfect knowledge of the plant inputs and in the presence of localized external heat sources of unknown values. To face these possible inconveniences, it was implemented a state augmentation of the original system to include a model of the unknown values inputs acting on the system and develop a linear KF based on that new model, an augmented KF. For the augmented state system, we assumed to know perfectly the nature of uncertain inputs.

In the bar model case, the plant inputs were 100% higher than those of the KFs. For this rather simple system, the use of only one sensor was enough to reach negligible estimation errors in this test, when the augmented KF is used, since the detectability of the augmented system is reached wherever the sensor is located. Moreover, with a right choice of the process noise covariance matrix,

and an appropriate location of the temperature sensor, it is possible to obtain an accurate estimate of the temperature trajectories, even before the steady state condition is reached. On the other hand, the classic KF was not capable of overcoming this huge input mismatches.

For the motor reduced order model test, the imposed differences between the plant and KFs input current was 10% (higher in the motor) while the ambient temperature difference was of 20% (also higher in the motor). The results were satisfactory implementing any of both the classic and augmented KF, with the help of two sensors. Both KFs are good enough estimating the temperature at one point in the motor shaft, another in the winding and a last one in the rotor external surface, reporting estimation errors smaller than 1% on each case. Even though the classic KF was not able to estimate correctly most of the states of the reduced order model, task that the augmented KF was able to perform satisfactorily, it was able to estimate with high accuracy the state of greatest importance (which is the one with the highest weight in the linear transformation from the reduced order space to the full order one).

Special attention has to be paid deciding both, the number of sensors and their location. In the motor case, the detectability of the augmented system was not granted with one sensor and one disturbance, because the considered sensor positions limited the observation degree of the system states. On the other hand, two sensors were sufficient to get smaller estimation errors implementing the augmented KF, than those obtained with the classic KF.

Increasing the number of disturbances to two and three, the augmented state KF was able to correctly estimate the temperatures for the bar case. With the right number of sensors and correctly positioning them, the estimation error was considerably smaller than 0.1%. In what regards the motor, the inclusion of two simultaneous input disturbances was studied as well, but the results were not satisfactory neither considering two nor three sensors, due to the not convenient location of them. In this sense, it is recommended to continue this study making systematic tests varying the number and positions of the sensors in order to asses if the augmented KF is useful in this case.

References

[1] B.D.O. Anderson and J.B. Moore. *Optimal Filtering*. Prentice-Hall, 1979.

[2] Peter Benner and Lihong Feng. "A Robust Algorithm for Parametric Model Order Reduction Based on Implicit Moment Matching". In: *Reduced Order Methods for Modeling and Computational Reduction*. Ed. by Alfio Quarteroni and Gianluigi Rozza. Cham: Springer International Publishing, 2014, pp. 159–185. ISBN: 978-3-319-02090-7. DOI: 10.1007/978-3-319-02090-7_6. URL: https://doi.org/10.1007/978-3-319-02090-7_6.

[3] Nicola Bianchi. *Calcolo delle Machine Electriche col Metodo degli Elementi Finiti*. CLEUP, 2001.

[4] Simon Dan. *Optimal State Estimation: Kalman, H Infinity, and Nonlinear Approaches*. Wiley-Interscience, 2006.

[5] Sandra Eriksson. "Permanent Magnet Synchronous Machines". In: *Energies* 12 (July 2019), p. 2830. DOI: 10.3390/en12142830.

[6] Daniel Fernandez et al. "Permanent magnet temperature estimation in PM synchronous motors using low cost hall effect sensors". In: *2016 IEEE Energy Conversion Congress and Exposition (ECCE)*. 2016, pp. 1–8. DOI: 10.1109/ECCE.2016.7855349.

[7] Gene F. Franklin, Michael L. Workman, and Dave Powell. *Digital Control of Dynamic Systems*. 3rd. USA: Addison-Wesley Longman Publishing Co., Inc., 1997. ISBN: 0201820544.

[8] Edward Glaessgen and David Stargel. "The digital twin paradigm for future NASA and U.S. air force vehicles". In: Apr. 2012. ISBN: 978-1-60086-937-2. DOI: 10.2514/6.2012-1818.

[9] Rudolph Emil Kalman. "A New Approach to Linear Filtering and Prediction Problems". In: *Transactions of the ASME–Journal of Basic Engineering* 82.Series D (1960), pp. 35–45.

[10] Byeong-Hwa Lee et al. "Temperature Estimation of IPMSM Using Thermal Equivalent Circuit". In: *IEEE Transactions on Magnetics* 48.11 (2012), pp. 2949–2952. DOI: 10.1109/TMAG.2012.2196503.

[11] Material Property Data MatWeb. *Aluminum, Al*. URL: https://www.matweb.com/search/datasheet.aspx?bassnum=AMEAL00&ckck=1.

[12] Kenneth R. Muske and Thomas A. Badgwell. "Disturbance modeling for offset-free linear model predictive control". In: *Journal of Process Control* 12.5 (2002), pp. 617–632. ISSN: 0959-1524. DOI: https://doi.org/10.1016/S0959-1524(01)00051-8. URL: https://www.sciencedirect.com/science/article/pii/S0959152401000518.

[13] Newtwen. *Internal Technical Report (private document)*. 2022.

[14] N. S. Ottosen and H. Petersson. *Introduction to the Finite Element Method*. Prentice Hall, 1992.

[15] Gabriele Pannocchia, Marco Gabiccini, and Alessio Artoni. "Offset-free MPC explained: novelties, subtleties, and applications". In: *IFAC-PapersOnLine* 48.23 (2015). 5th IFAC Conference on Nonlinear Model Predictive Control NMPC 2015, pp. 342–351. ISSN: 2405-8963. DOI: https://doi.org/10.1016/j.ifacol.2015.11.304. URL: https://www.sciencedirect.com/science/article/pii/S2405896315025884.

[16] Gabriele Pannocchia and James Rawlings. "Disturbance Models for Offset-Free Model-Predictive Control". In: *AIChE Journal* 49 (Feb. 2003), pp. 426–437. DOI: 10.1002/aic.690490213.

[17] Gregory Plett. *Battery Management Systems, Volume II: Equivalent-Circuit Methods*. Vol. 2. 2015.

[18] Gregory Plett. "Extended Kalman filtering for battery management systems of LiPB-based HEV battery packs: Part 1. Background". In: *Journal of Power Sources* 134.2 (2004), pp. 252–261. ISSN: 0378-7753. DOI: https://doi.org/10.1016/j.jpowsour.2004.02.031. URL: https://www.sciencedirect.com/science/article/pii/S0378775304003593.

[19] Danish Rafiq and Mohammad Abid Bazaz. "Model Order Reduction via Moment-Matching: A State of the Art Review". In: *Archives of Computational Methods in Engineering* 29.2 (2022), pp. 1463–1483. DOI: 10.1007/s11831-021-09618-2. URL: https://doi.org/10.1007/s11831-021-09618-2.

[20] Andreas Specht and Joachim Böcker. "Observer for the rotor temperature of IPMSM". In: *Proceedings of 14th International Power Electronics and Motion Control Conference EPE-PEMC 2010*. 2010, T4-12-T4–15. DOI: 10.1109/EPEPEMC.2010.5606818.

[21] Francesco Toso et al. "Digital Twins as Electric Motor Soft-Sensors in the Automotive Industry". In: *2021 IEEE International Workshop on Metrology for Automotive (MetroAutomotive)*. 2021, pp. 13–18. DOI: 10.1109/MetroAutomotive50197.2021.9502885.

[22] Oliver Wallscheid. "Thermal Monitoring of Electric Motors: State-of-the-Art Review and Future Challenges". In: *IEEE Open Journal of Industry Applications* 2 (2021), pp. 204–223. DOI: 10.1109/OJIA.2021.3091870.